Holocene environmental change in Rotsee, and its impact on sedimentary carbon storage

Cindy De Jonge[1*], Nathalie Dubois[2], Nemiah Ladd[3], Longhui Deng [4], Niroshan Gajendra [4,5], Negar Haghipour [1, 6], Carsten J. Schubert[4, 7], Mark Lever[4, 8]

[1] Geological Institute, ETH Zurich, Sonneggstrasse 5, 8092 Zurich, Switzerland
[2] Department of Surface Waters Research and Management, Eawag, Uberlandstrasse 133, 8600 Dubendorf, Switzerland.
[3] Department of Environmental Sciences, University of Basel, Bernoullistrasse 30/32, 4056 Basel, Switzerland
[4] Institute of Biogeochemistry and Pollutant Dynamics, ETH Zurich, Universitaetstrasse 16, 8092 Zurich, Switzerland
[5] Currently at: Institute for Energy Technology (IFE), Instituttveien 18, 2007 Kjeller, Norway
[6] Laboratory of Ion Beam Physics, ETH Zurich, Otto-Stern-Weg 5, 8093 Zürich, Switzerland.
[7] Department of Surface Waters, EAWAG, Swiss Federal Institute of Aquatic Science and Technology, Kastanienbaum, Switzerland.
[8] Currently at: Marine Science Institute, University of Texas at Austin, 750 Channel View Drive, Port Aransas, TX 78373, USA.

*Corresponding author: C. De Jonge
C. De Jonge: cindy.dejonge@eaps.ethz.ch *
N. Dubois: nathalie.dubois@eawag.ch
N. Ladd: n.ladd@unibas.ch
L. Deng: longhui.deng@sjtu.edu.cn
N. Gajendra: gajendra.science@gmail.com
N. Haghipour: negar.haghipour@eaps.ethz.ch
C. J. Schubert: carsten.schubert@eawag.ch
M. Lever: mark.lever@austin.utexas.edu

Keywords: Holocene, Lake system evolution, Sedimentary carbon, Ancient DNA, Py-GC/MS, Provenance

Abstract

To assess the long-term impact of climate change on mountain lakes and their sedimentary carbon storage, paleo-environmental approaches using well-dated lake sediment cores can be employed. For Rotsee, a perialpine lake near the Swiss Alps, a new sediment core has allowed the reconstruction of carbon mass accumulation rates for organic and inorganic carbon since 13ka BP. A multiproxy approach (XRF, carbon and nitrogen isotopes, organic macromolecule chemical compositions, and aDNA) was used to explore changes in the lake system that affect sedimentary carbon storage. Early Holocene warming led to a stepwise increase in inorganic carbon deposition, while organic carbon accumulation gradually increased throughout this period. Despite apparently affecting phytoplankton community proxies, warming during the Holocene Thermal Maximum did not directly impact sedimentary carbon storage. In the mid-Holocene, gradual lake infill caused shallowing and changes in water chemistry, redox conditions, and sources of organic matter. During this period, the sedimentary record indicates low pH, anoxic waters, and an influx of allochthonous, plant-derived organic matter, which increased organic carbon storage while inorganic carbon became negligible. In the Late Holocene, climatic or land use changes deepened the lake, leading to a more oxidized water column and a decline in allochthonous organic matter input. Still, larger deforestation events, such as during Roman times, coincided with increased organic carbon storage. Recent sediments, influenced by eutrophication in the last century, show intermediate carbon accumulation rates compared to earlier Holocene periods. Rotsee serves as a case study of how climate warming has influenced lake development and sedimentary carbon storage, with broader implications for understanding carbon dynamics in high-alpine lakes and their future carbon balance.

Introduction (body of text: 7303 words)

Present-day climatic changes impact highly sensitive alpine and subalpine lake ecosystems, their sediment composition and carbon storage potential (Moser et al. 2019). With increasing temperatures and glacier retreat, increased growth of vegetation and soil development (reviewed in Trautmann et al. 2023), the enhanced transfer of nutrients by leaching or deposition can cause future increases in lake trophic state (Pastorino et al. 2024). This climate-related eutrophication, as well as anthropogenically-driven eutrophication, have already increased storage of organic carbon in lake surface sediments (Anderson et al. 2014; Fiskal et al. 2019). Still, with increased temperature impacting both the production and respiration of carbon (Gudasz et al. 2010), it remains difficult to predict whether lake sediments will be a future source or sink of carbon. Lake sediments that cover the last centuries to millennia have been shown to be excellent archives of past responses of sedimentary carbon on climatic and land-use changes (Moser et al. 2019).

In the last 14 ka, the Alps and their foreland have experienced several stages of climate variability. This started with the continued warming following the last glacial maximum (22.2 ± 1.0 ka, Reber et al. 2014), which caused extensive foreland glaciers to recede. The variability in temperature and associated ecological impacts of the Bolling-Allerød interstadial and colder Younger Dryas stadial are well-recorded in lake sediments (e.g. Moscariello et al. 1998; Lotter et al. 2000; Samartin et al. 2012; Hoehn et al. 2022). The Younger Dryas was followed by the Holocene, a period of relative climate stability. Vegetation reconstructions and treeline changes suggest the early and mid-Holocene were relatively warm (Wick and Tinner 1997; Nicolussi et al. 2005). This period, referred to as the Holocene Thermal Maximum (HTM), has been recognized in several studies (e.g. Renssen et al. 2012). The exact timing of the HTM is debated but studies propose it occurred from 7.5-5.9 ka BP in Austria (Vollweiler et al. 2006), or from 9.8 to 6.4 ka BP, with an intermittent cold episode from 8.8 to 7.8 ka BP, in Switzerland (Affolter et al. 2019).

These well-described past climate changes left an imprint on lacustrine sediments. For instance, warming, resulting in a lake level drop, has been identified as a past cause of eutrophication in Lake Lobsigen in the early Holocene (Ammann 1986). Climate changes impact lake sediments by the development of shoreline peat or vegetation (Ammann 1986) and/or lake infilling (Heiri and Lotter 2003). While this is a natural stage in the succession of a freshwater system, enhanced infilling and eutrophication can also be the consequence of human activities (Ammann 1986; Heiri and Lotter 2003), such as increased sewage input (e.g. Hasler 1947, Fiskal et al. 2019), or increased outwash of nutrients due to soil erosion following deforestation (e.g. Haas et al. 2019). In the Swiss alpine realm reconstructed vegetation dynamics indicate that anthropogenic deforestation started having a substantial impact around 5 ka BP (Wick and Tinner 1997, Nicolussi et al. 2005), and subsequently increased carbon storage in lake sediments (Kastowski et al. 2011).

In the Swiss foreland region, lakes formed during the retreat of the large Reuss, Rhine and Linth glaciers have recorded the large ecological changes following post-glacial warming in their sedimentary records. Rotsee is a small, monomictic lake (0.48 km^2) in the Swiss alpine foreland that was formed after the retreat of the Reuss glacier. The development of Rotsee started as early as 14.6 ka BP, as suggested by the age of a terrestrial macrofossil (C823, 14570 ± 240 cal ^{14}C age) from a shoreline peat core (Lotter 1988). Initial sedimentological and paleo-ecological descriptions of Rotsee sediments were based on pollen, plant macrofossils, diatom frustules, and stable isotopes (Lotter 1988; 1989). Late glacial and early Holocene climate (Verbruggen et al. 2010) and hypolimnion oxygen availability was subsequently based on oxygen isotopes (Ursenbacher et al. 2020). These studies show that Rotsee sediments record a well-expressed late glacial interstadial (Bølling–Allerød: 14 650 - 12 860 cal a BP), Younger Dryas (12 860 - 11 610 cal a BP) and early Holocene (<11 610 cal a BP). At the Younger Dryas/Holocene transition, up to 4 °C of warming during the summer, i.e. the period of carbonate precipitation, has been reconstructed (Verbruggen et al. 2010). The age boundaries of the HTM (pollen zones VI and VII in Lotter 1988) were found to agree with previously determined boundaries (8 to 5 ka BP; Welten 1982). Concerning lake system changes, Lotter 1989 describes a system that was originally deep and oligotrophic, and gradually became more eutrophic as the soils in the surrounding watershed developed. Rotsee also became shallower as the lake filled in, with the development of extensive shoreline Alder Carr vegetation starting at 7 cal ka BP (Lotter 1988). In spite of the early oligotrophic conditions, chironomid relative abundances show that already during the Younger Dryas and earliest Holocene, the hypolimnion had decreased oxygen availability (Ursenbacher et al. 2020), a condition that was also reported for the last 2 ka (Lotter 1989, Zuellig and Rheineck 1985). Rotsee sediments started to show indications of direct human impact around 2.5 ka BP, following deforestation in the watershed by Roman settlers (Lotter 1989). More recently, following the increase in untreated wastewater input after 1850 (Stadelmann 1980), Rotsee became highly eutrophic. This resulted in the formation of a seasonally anoxic deep water column, as indicated by okenone, a biomarker lipid for purple sulfur bacteria (Zuellig and Rheineck 1985).

Because of its long record of climate, vegetation successional, and anthropogenic changes, Rotsee sediments provide an excellent opportunity to investigate how these changes affect the long-term burial and preservation of sedimentary carbon pools. Based on a multiproxy approach we here test the hypothesis that climate warming from the late glacial to the early Holocene contributed to an increase in trophic state, primary productivity and associated organic carbon accumulation rates in Rotsee. We furthermore postulate that this increase was further accelerated by trophic state alterations due to anthropogenic land-use changes, which ultimately more significantly affected carbon storage than natural climatic shifts.

Methods

Core collection and on-site subsampling

Three short cores and two long cores were collected at a water depth of 5.5 m (47°04’27.81”N, 8°19’25.7”E WGS 84; 667230/214087 LV95) between 03/10/2021 and 05/10/2021. The short cores (40-60 cm long) were collected from a vessel using a gravity corer with clear plastic liners (UWITEC; inner liner diameter 90 mm). The two long cores (sections ROT21-1-1 to ROT21-1-5 and ROT21-1-6 to ROT21-1-9) were taken 4 m apart from each other, using a shoreline moored platform using a piston coring system with a manual hammer, without a re-entry cone (UWITEC; inner liner diameter: 59.5 mm). Long cores were taken in sections of 3 m (except for 1 section that was 2 m). The recovery of two parallel long cores, vertically offset by one meter, was necessary to obtain a high-quality, complete sedimentary sequence. All short and long cores were brought on-shore for sampling immediately after core recovery. Short cores were maintained in vertical position and sampled by extrusion, whereas long cores were first accessed horizontally through ‘windows’ that were cut into the core liner. From each depth sampled, sediments for DNA analyses and macromolecular organic matter analyses were collected with sterile cut-off syringes. Samples for DNA extraction were immediately frozen in liquid N_2, before storage at -80 °C, whereas samples for organic matter analysis were frozen and stored at -20 °C. Afterwards, the core sections were split lengthwise before subsampling 2 cm slots for bulk carbon and nitrogen analyses using solvent cleaned spatulas. One core half (so-called archive half) remained intact for imaging and XRF scanning.

XRF scanning

Elemental compositions were measured at 5 mm resolution using a µXRF core scanner (Avaatech XRF) with an Oxford 100 W X-Ray tube and a rhodium anode equipped with a Canberra X - PIPS/DSA 1000 (MCA) detector. Prior to analysis, core surfaces were flattened to ensure uniform scanning and covered with 4 µm Ultralene foil. Elemental groups with lower energy levels were measured at 10 kV (1500 A, no filter, 15 s exposure), while mid-energy groups were measured at 30 kV (2000 A, Pd thin filter, 40 s exposure). In addition to the cps counts (Supp. Fig. 2), selected XRF ratios were calculated.

Dating and age model

The top 50 cm of a short core was sectioned at 1 cm resolution and used for ^{210}Pb and ^{137}Cs dating (Fig. 1A; Supp. Table 1A). ^{137}Cs peaks were determined to date the sediment layers deposited in 1987 and 1963 AD. In addition, radiocarbon dating on 19 macrofossils, including 12 seeds, leaf remains and twigs of terrestrial plants, and 7 macrodetrital remains of aquatic macrophytes was performed (Supp. Table 1B). After wet sieving, macrofossils were subjected to a room temperature acid-alkali-acid treatment (Norris et al. 2020) to remove carbonates, acid soluble humic material, and humic acids. At two depths, bulk sediments were acidified using fumigation (described in Haas et al. 2019) and weighed in for ^{14}C dating, with the aim of constraining the reservoir age during the Younger Dryas (Supp. Table 1C). ^{14}C measurements were carried out on an Accelerator Mass Spectrometer (AMS) with an Elemental Analyzer unit (EA) using the MIni CArbon DAting System (MICADAS) at the Laboratory for Ion Beam Physics of the Eidgenössische Technische Hochschule (ETH) in Zurich. An age-depth model was created using rplum, which allows unsupported ^{210}Pb, ^{137}Cs and uncalibrated ^{14}C ages to be combined based on Bayesian statistics (Blaauw and Christen 2011). Radon measurements are available as estimates of supported Pb-210, assumed constant by the model. A memory strength of 10 and memory mean of 0.5 is used. In this model, ^{14}C ages are converted to calendar ages using the INtCal20 calibration curve (Reimer et al. 2020).

Bulk nitrogen and carbon content and isotopes

Sediments were freeze-dried and homogenized using an agate mortar and pestle. Total nitrogen (%; TN) and $\delta^{15}N_{-TN}$ values were determined on unacidified sediments using an EA-IRMS system composed of a Vario Pyro Cube coupled to a Isoprime 100 IRMS (Elementar, Germany). Repeated measurement of reference materials Acetanilide #1 (Schimmelmann, USA, $\delta^{15}N = +1.18 \pm 0.02$) and High Organic Sediment Standard (HEKAtech, Germany, $\delta^{15}N = +4.32 \pm 0.20$) were used to determine the instrument precision, which was determined to be generally below 0.05 ‰ $\delta^{15}N$ for the Acetanilide standard, and below 0.07 ‰ $\delta^{15}N$ for the sediment standard. Offsets between the measured and known $\delta^{15}N$ values of the Acetanilide standard (average offset = 0.19 ± 0.08) were used to correct the $\delta^{15}N_{-TN}$ values of the bulk sediments. The contents of total carbon (TC), total organic (TOC) and total inorganic (TIC) carbon were measured on the SoliTOC® Cube (Elementar Analysensysteme, Germany). The reported TOC is the summed amounts of TOC400 and refractory organic carbon (ROC), with TOC400 determined at 400 °C and ROC between 400 °C and 600 °C, and TIC between 600 °C and 900 °C. Low (B2152) and high organic carbon content standards (B2150) from Elemental Microanalysis (United Kingdom) were run with each batch to determine the instrument accuracy, which was determined to be 98.9 ± 0.6%. $\delta^{13}C_{-TOC}$ of bulk sediments was measured on an EA-IRMS system, EA Vario Pyro Cube (Elementar Analysensysteme, Germany) and Isoprime IRMS (GV Instruments, UK), after acidification. For acidification, samples with inorganic carbon were subjected to a 1N HCl treatment until no more visible reaction occurred. To calibrate the instrument an Acetanilide #1 (Schimmelmann, USA, $\delta^{13}C$ = -29.52 ± 0.01) standard was used, as well as a High Organic Content Sediment (SA990894; $\delta^{13}C$ = -28.85 ± 0.10) and Low Organic Soil (SA33802152; $\delta^{13}C$ = -22.88 ± 0.10) standards from Hekatech Analytics. In general, instrument precision during the runs was below 0.06 ‰ $\delta^{13}C$ for Acetanilide and below 0.16 ‰ $\delta^{13}C$ for the sediment and soil standard, and an accuracy above 0.02 for $\delta^{13}C$ for Acetanilide and 0.1 ‰ $\delta^{13}C$ for the sediment and soil standard. No corrections of the $\delta^{13}C$ values were performed.

Bulk compound classes and hydrocarbons

To determine the OM macro-molecular composition, pyrolysis gas chromatography mass spectrometry was used, following the set-up as described in Gajendra et al. 2023. The pyrolizer was connected to an autosampler (PY-2020iD and AS-1020E, FrontierLabs, Japan) and to a GC/MS system (Trace 1310, Thermo Scientific and ISQ 7000, Thermo Scientific) equipped with a DB-5MS capillary column (30 m x 0.25 mm i. d., 0.25 mm film thickness; J&W, Agilent Technologies AB, Sweden). Chromatograms were analyzed in R (version 2.15.2, 64 bits) based on a pipeline that identifies common mass fragments as pyrolysis products (Tolu et al. 2015). Pyrolysis products were then classified and annotated according to Tolu et al. (2015) and Ninnes et al. (2017). Areas of individual compounds within each compound class were summed (Supp. Table 2 for identity of individual compounds), and compound classes expressed as relative abundances (peak area of each compound class relative to total characterizable Py-GC/MS peak area).

Mass accumulation rates

Dry bulk density values were not measured directly on the sediments but were calculated based on the modeled value for weighed average particle density (Avnimelech et al. 2001) and the interpolated measured porosity values (n = 68; based on weights of 20-mL sediment volumes before and after freeze-drying), using the linterp command from the astrochron package (Meyers 2014) at a 1 cm resolution. For the percentage of organic matter, TOC was multiplied by a factor of 1.7, following a conventional conversion proposed by Brady, 1984 (Brady and Weil 2016). Mass accumulation rates (MAR) were then calculated by multiplying the modeled dry bulk density with percentages of TOC, TIC, and normalized per year, using a smoothed sedimentation rate (autoplot, smoothing with a Gaussian kernel set to 25) using the astrochron package (Meyers 2014).

aDNA analysis

Sedimentary DNA was extracted according to Lysis Protocol I of Lever et al. 2015. Briefly, 0.2 g of sediment was added to 2-mL screw-cap tubes filled to 15 % with 0.1 mm Zr beads. For the vast majority of samples, 100 µl of 10 mM adenosine triphosphate (ATP; prepared by dissolving adenosine 5’-triphosphate disodium trihydrate in molecular grade water) solution was added to reduce DNA sorption. The only exceptions were deep glacial clay layers, in which recovery was significantly enhanced by increasing the ATP concentration to 300 mM. 0.5 ml of lysis solution I was added (Lever et al. 2015). Samples were then shaken for one hour at 50 °C (600 rpm; ThermoShaker, Eppendorf), and subsequently washed twice with cold 24:1 chloroform-isoamyl alcohol and precipitated with linear polyacrylamide (20 µg ml^{-1}), 5 M sodium chloride and ethanol. The pellets were dried using a vacuum centrifuge (50 °C; Thermo Fisher Scientific, USA), resuspended in molecular grade water and purified with the CleanAll DNA/RNA Clean-up and Concentration Micro Kit (Norgen Biotek Corp., Canada; Protocol A). All extracts of samples and extraction negative controls (extraction blanks) were stored at -80 °C. Eukaryotic 18S rRNA and rbcL genes were quantified by real-time PCR (Lightcycler® 480; Roche) with SYBR®Green as dye. Eukaryotic 18S rRNA genes were amplified using the All18S primer pair (Deng et al. 2020), whereas chloroplast genes encoding the large subunit of ribulose-1,5bisphosphate carboxylase (rbcL) were quantified using published assays for vascular plants (Willerslev et al. 2003), Chlorophyta and Ochrophyta (both Han et al. 2022).

Results

Core description and age model

The first (core section ROT21-1-1 to ROT21-1-4) and second borehole (core sections ROT21-1-5 to ROT21-1-8) were aligned based on 25 tie points of the XRF traces Zr, Co, Ca, P/Ti and Ca/Ti. The alignment allowed 5-20 cm sediment sections at the top of each 3m section to be identified as infill; these sediment layers were removed from further analysis. Based on the compiled core ROT21-1, the sedimentary record of Rotsee has 3 lithological units (Fig. 1A), that reflect sudden changes in lithology. The deepest section (Unit C) consists of a homogenous clayey deposit of 2.8 m, which is overlaid by a narrow section (70 cm; Unit B) of banded sediments, composed of light-colored clayey sediments, interspersed with dark-colored layers of well-preserved macrophyte material and organic-rich sediments (gyttja). Unit A represents a period of continuous sedimentation, composed of 4.5 m of non-varved calcareous gyttja (Unit A3), gradually changing into 4 m of non-varved non-calcareous gyttja (Unit A2), with the surface 1 m showing a gradual return to calcareous gyttja (Unit A1). The general core description matches the composition of core RL-240 and RL-250 taken in the year 1985, described by Lotter 1988 with some notable differences. For instance, the Laacher See Tephra was described in core LR-250 at 776 cm depth below lake floor (blf) but was not recognized at our site. On the other hand, layers of macrophyte material (present in Unit B) were not encountered in the older cores.

The Bayesian age model (Fig. 1A) shows that the top 1024 cm (Unit A-B) cover the last 13 cal ka BP (± 0.35ka), with 'present' defined as the year 1950. Within Unit B several reversals of non-calibrated ^{14}C ages are documented, on the order of 70 to 400 years. However, these age offsets do not exceed the summed error of the estimated ages, which is composed of the measurement error, and the error inherited from the reservoir age correction (after Soulet, 2015; Supp. Table 1C), and are therefore not interpreted as sediment reversals. Within Unit A, 9 of the 12 dated plant macrofossils overlap with the 95 % confidence interval of the age-depth model. The top of the composite profile is determined by the alignment of the short core XRF profile. Based on a Bayesian model of ^{210}Pb activities, where unsupported ^{210}Pb was calculated by subtracting ^{226}Ra activity from total ^{210}Pb, an age of 0 yr is modeled at 8.5 cm depth. While the radio-isotopic profile for ^{210}Pb generally follows the expected exponential ^{210}Pb decay, sediments deposited between 2 and 5 cm depth have a decreased ^{210}Pb activity (Fig. 1A). A decrease of ^{210}Pb activity in recent sediments has been described before (Baud et al. 2023) and has been partially explained by eutrophication and/or acidification of the lake. Since the sediment ages based on the ^{210}Pb model and two identified ^{137}Cs peaks (Supp. Table 1) match, sediments above 8.5 cm depth are interpreted to reflect modern material. Sedimentation rates (Fig. 1B) are on average 0.8 mm * yr^{-1}, with notable increases to ~1.5 mm*yr^{-1} between 9.5 and 5.9 cal ka BP and since 500 cal a BP, and shorter, i.e., multi-century, increases around 4.1 and 1.5 cal ka BP (Fig. 1B).

Based on the timing of previously published climate reversals at Rotsee, Unit C is thus contemporary with the deposition of clays during the last Glacial Interstadial, Unit B was deposited during the Younger Dryas (12976 ± 354 to 11775 ± 340 cal a BP), and Unit A covers the Holocene, with Unit A2 deposited during the Mid- to Late Holocene (834 ± 221 to 7034 ± 199 cal a BP).

Sedimentary composition with depth

Total inorganic carbon (TIC) and total organic carbon (TOC) show a large downcore variation in dry weight percent (1.6 to 28 % for TOC, 1.8 to 12 % for TIC; Fig. 2). In Unit C, Total Carbon (TC) is represented almost entirely by inorganic carbon, which reaches up to 4 % (dry sediment weight). Unit B shows strong fluctuations in TOC and TIC, with TIC and TOC reaching 10 and 25 % respectively, In the transition to A3, TIC increases and TOC decreases again, only to be followed by a gradual increase in TOC (from 5% to 25%) and decrease in TIC (from ~12% to <0.5%) throughout A3. Unit A2 sediments contain almost exclusively by TOC, with values of 15 to 25% except for a decrease to 5% in the transition to A1. In A1, TOC remains at the current values of 5 %, and TIC increases to values of 2 to 5%.

To further investigate changes in the sedimentary composition with depth, the elemental composition was characterized by XRF scanning. Different sources of variability are reflected by the scores on the principal component axes (Supp. Fig. 1). PC1 (Fig. 2B) is mainly driven by variations in the contents of terrigenous (Ti, K, Al, Si, Fe and Mg) and trace elements (Ga, Rb, Y; Supp. Fig 1) that indicate varying contributions of fine-grained clastic material. Accordingly, inputs of clastic material were high in Unit C, matching the dominance of glacial clays, were generally low throughout Units B A3, and most of A2, and increased again in the top sediments of Unit A2 (140 cm) and A1. Complementary analyses of Ti/Al ratios are generally interpreted as a proxy for gain size, with Ti reflecting larger grain sizes (i.e. Zhao et al. 2011). Sedimentary increases in Ti/Al ratio values are generally interpreted to respond to an increase in grain sizes following land use changes (soil erosion, i.e. Olsen et al. 2010), or an increase in terrigenous riverine input (Lim et al. 2019). At Rotsee, low values are encountered in the glacial clay layer in Unit C (Fig. 1A). Throughout Units B and A, Ti/Al values increase gradually, reaching maximum values towards the top of A2. Notably, there is no correlation between Ti/Al values and the amount of siliciclastic material as captured by PC1 values (r=-0.01, p=0.94).

The second principal component (PC2) is driven by variations in Ca, Sr and Cr, with bio-essential trace elements such as Co, Ni showing opposite loadings on PC2 (Supp. Fig. 1). Downcore PC2 values generally follow the TIC content. PC2 is interpreted to reflect variations in the sedimentary calcium carbonate (calcite) content, with Sr being a common trace element in calcite and Cr often co-absorbed to calcite. Matching the inorganic carbon values, PC2 values are intermediate in glacial clays (Unit C), and mostly increase throughout Unit B, reaching their highest values at the base of A3, before they decrease to low values (A2) and increase again in the most recent sediments (Unit A1). The orthogonal variation to PC1 and lack of correlation with Ti/Al indicate that PC2 is not driven by clastic material. Instead, PC2 can be interpreted as a parameter for calcite produced either by calcifying phytoplankton (biotic), or precipitated abiotically during phytoplankton blooms. PC2 is correlated with Ca/Ti (r=0.87, p¡0.001) and Si/Ti ratios (Fig. 2), indicating that these ratios capture biogenic calcite and silica, respectively, and can be used to reconstruct changes in primary productivity, as shown previously by Liu et al. (2013). Detrital inputs of Ca-bearing minerals are generally of minor importance, and at least in recent periods, the carbonate content of Rotsee was a good proxy for primary productivity (Lotter 1989). The bulk of Si delivered to lakes is bio-available, and diatoms precipitate the bulk of dissolved Si in Swiss lakes (Lake Lugano; Hofmann et al. 2002). As diatom valve counts of up to $10 * 10^6$ valves per g dry weight have been recorded in Rotsee (Lotter 1988) we assume that the bulk of the silica as estimated by the Si/Ti ratio is biogenic silica.

XRF ratios of redox-sensitive elements Mn and Fe (Fe/Ti, Mn/Fe) show most variability within Unit A2 (Fig. 2). Here, the presence of a seasonally anoxic hypolimnion or the presence of metal complexes with humic substances (Makri et al. 2021) can result in increased ratio values. Fe/Ti ratios are generally elevated in Unit A2, with a local maximum between 260 and 300 cm blf and a smaller excursion at 344-354 cm (both in Unit A2). Similarly, local peaks in Mn/Fe ratio values were present between 170-410 cm, with decreased values between 200-305 cm, at those depths where an increase in the Fe/Ti values is observed. P/Ti traces the sedimentary phosphorus and is weakly correlated with Fe/Ti (r= 0.17, $p \leq 0.05$). Fe/Ti ratios were interpreted as a proxy for seasonal bottom water anoxia (Davison 1993). Elevated Mn/Fe ratios have previously been interpreted to indicate periods with relatively more oxic bottom water conditions (i.e. a short anoxic season; Davison 1993) or extended hypoxic conditions (e.g. Jones and Bowser 1978).

Carbon accumulation rate and provenance through time

The large changes in TIC and TOC content result in variable individual mass accumulation rates (MARs) of organic and inorganic carbon through time (Supp. Fig. 3; Fig. 3B). The inorganic carbon MAR becomes substantial only in early Holocene sediments with a sustained maximum of 400 g*m^{-2}*yr+ between 10.4-10.9 ± 0.25 cal ka BP. Afterwards, it decreases throughout Unit A3, with no accumulation of inorganic carbon in Unit A2. Intermediary inorganic carbon MAR values are observed in Unit A1 (Fig. 3B). Organic carbon MARs are intermediate in Unit A3 and A1, reaching a sustained maximum of 500 g*m^{-2}*yr^{-1} late in Unit A3 between 7.0 and 7.3 ± 0.2 cal ka BP, and within Unit A2 between 4.3 and 4.9 ± 0.2 cal ka BP and between 1.6 and 2.1 ± 0.18 cal ka BP. The total carbon accumulation rate is highest in Unit A3 (up to 755 g*m^{-2}*yr^{-1} at 10.8-10.95 ± 0.25 cal ka BP; Fig. 3B). The composition of organic matter can be described with TOC/TN values (Fig. 3C), that are lowest in glacial clays (≤7), and generally increase throughout Unit B (~12), with high TOC/TN variability in Unit B and high values (≥15) recorded in an individual organic carbon poor layer (Fig. 3). Lacustrine sediments (Unit A) generally have intermediate TOC/TN values (6-15). Bulk $\delta^{13}C_{\text{-TOC}}$ values show low values in Unit B, afterwards gradual increase to -28 ‰, with generally low variability in Unit A (Fig. 3D). The TOC/TN and bulk $\delta^{13}C_{\text{-TOC}}$ values are contrasted in Supp. Fig. 4B. Bulk $\delta^{15}N_{\text{-TN}}$ (Fig. 3E) has a minimum (~0 ‰) value in the upper half of Unit A3, showing a gradual increase to values of 2 ‰ in Unit A2 and of 5 ‰ in Unit A1. The increase is most pronounced in sediments shallower than 175 cm blf.

The fractional abundances of macromolecular components are reported, in the framework of sediment units A-C and the known climate zones (Fig. 4). The main variation is caused by an increase in the fractional abundance of esters and fatty acids in surface sediments (PC1; Supp. Fig. 5). Fatty acids represent 27-35 % at 5-9 cm blf (modern sediments), and esters representing 13-32 % of organic matter above 22cm blf (60 ± 2 cal a BP; Fig. 4). N-compounds show a maximum (19 %) at 60 cm blf (28 ± 97 cal a BP). The second direction of variation concerns lignin, phenol and chlorophyll compounds that anti-correlate with N-containing compounds and carbohydrates, showing substantial variation across the whole core (PC2; Supp. Fig. 5). Clay sediments (Unit C) have a distinct macromolecular composition, characterized by either increased fatty acids or PAHs and aldehydes (13798 ± 722 cal a BP and older). Lacustrine sediments overlying this section, show an increase in carbohydrates can be attributed to an increase in furanones, pyrans, chitin-derived sugars, methyl-α-d-ribofuranoside and dianhydrorhamnose (Fig. 4). Only in the lacustrine sediments from Unit A, contributions of lignin (0.7-1.4 %; section A2-A3) and chlorophyll (2-4 %; section A2-A3) and increased contributions of phenols (22-

39 %; section A2-A3) are observed. Phenols become especially abundant compounds (30-39 %) in sediments deposited between 3200 and 6600 cal 14C a BP (n=3). Fig. 3G shows the concentration of quantified 18S rDNA and rbcL genes, that each represent a specific range of the composition of sedimentary DNA. These labile compounds show a strong initial decrease with depth, with both 18S rRNA and rbcL genes concentrations increased (100 to 10000-fold for Eukaryotes and Ochrophyta respectively) in the most surficial sediment layers (0-10 cm). A subsurface maximum is present in sediments that were deposited in the last 50 cal a BP years (12 ± 13 for Chlorophyta, 0 ± 10 for Eukaryotes and -11 ± 8 for Tracheophyta, in cal a BP). After the initial decrease in concentration in the last 100 years, counts of eukaryotic DNA remain stable throughout the core. 18S rRNA genes from Eukaryotes are found conserved in sediments of over 14ka old (Unit C to Unit A1), with rbcL genes found in sediments from over 12ka (Unit B to Unit A1). The gene ratio of Tracheophyta, Chlorophyta and Ochrophyta rbcL genes and 18 S rRNA genes is plotted in Fig. 4 to allow comparison with the macromolecular composition. In the early Holocene, the gene ratio of Tracheophyta increases in pace with the compound groups of phenols, lignins and chlorophylls. Chlorophyta rbcL genes show a relative increase in the late Holocene, when N-containing compounds and carbohydrates are increased. Ochrophyta rbcL genes show an increase in the most recent sediments, with a maximum at 15 cm blf (-39 ± 1 cal a BP, 1989 AD).

Discussion

The impact of climate warming on ecological succession and carbon content in the early and middle Holocene

Successional and trophic changes in the young Rotsee system

Climate warming from the Late Glacial to the middle Holocene causes marked changes in sedimentary carbon (Fig. 3), due to changes in lake system and trophic state. In the glacial clays, which are characterized by high inorganic and low organic carbon content, the TOC/TN ratio values and bulk $\delta^{13}C_{-TOC}$ values (Supp. Fig. 4) reflect an organic matter provenance that is dominated by bacterial biomass, while the absence of aromatic lignin and phenol compounds (Fig. 4), implies the absence of extensive vegetation around Rotsee in this period (e.g. Bader 1957). PAHs are present, tentatively interpreted to derive from grassy vegetation fires. Remarkably, labile compounds are also encountered, specifically esters, fatty acids and aldehydes. This reflects either active microbial activity in the glacial clays, or the good preservation of organic matter that was deposited over 13 cal ka ago. Glacial mass accumulation rates of carbon are not constrained, but are expected to be low, based on potentially high accumulation rates and low TOC and TIC content.

During the Younger Dryas, the presence of distinct layers of *Characeae* sp., coeval with a decrease in the supply of glacial clays (Fig. 2B), attest to clear water conditions, allowing the development of macrophytes. Increased amounts of S, Ni, Br, Cu, As and U (Supp. Fig. 2) are indicative of the potential of Chara to bio-accumulate these metals from the water column (Marchand et al. 2010). The well-preserved layers of macrophyte organic matter reflect anoxic conditions at deposition. This can be either caused by a sudden onset of anoxia, potentially caused by a burial event, or the deposition of macrophyte material in an anoxic hypolimnion after transport. Within the YD, low oxygen conditions in Rotsee were previously reconstructed based on chitinous invertebrate remains (Ursenbacher et al. 2020). Because of the high porosity values in the layers of macrophyte biomass (larger than unity), the calculated mass accumulation ranges of macrophyte biomass-derived C in the Younger Dryas is low (Fig. 3B). Furthermore, as not all sediment cores collected in Rotsee contain this material (Lotter 1988), its preservation is probably limited to local deposition centers.

Following the end of the Younger Dryas, continuous lacustrine sedimentation is observed throughout the Holocene, characterized by an increasing fraction of organic carbon (Fig. 2A) during the early and middle Holocene, reflecting the expected increase in trophic state. Inorganic carbon deposition rates of up to 600 $g*m^{-2}*yr^{-1}$ are observed (Fig. 3B), coeval with increasing values of Ca/Ti and Si/Ti, reflecting a shift from macrophyte dominated to phytoplankton dominated lake system. Mass accumulation rates of organic carbon, varying between 56 and 600 $g*m^{-2}*yr^{-1}$, are high throughout the early Holocene. The HTM seems to stimulate productivity further, as biomass derived from cyanobacterial blooms (Fig. 3E, $\delta^{15}N_{-TN}$ = 0.5 ‰; Teranes and Bernasconi 2000), indicative of nitrogen limitation, are limited in time to the HTM periods. Phytoplankton aDNA also supports the interpretation that HTM periods are characterized by a change in primary producers compared with background early Holocene conditions, with Ochrophyta (dominantly reflecting diatoms in Rotsee, in parallel with Han et al. 2022) and Chlorophyta aDNA generally absent during warm periods. The HTM periods are however not characterized by increased organic carbon MAR rates (Fig. 3B). The climate warming from the late glacial to early Holocene thus resulted in a phytoplankton dominated system, with an increase in sedimentary carbon storage, initially as inorganic carbon, with a gradual increase of the organic matter fraction. Rotsee thus supports the hypothesis that climate warming that allows lake development results in increased carbon storage. On the longer term (millennia), the type of sedimentary carbon changes significantly, and successional changes need to be taken into account.

Sedimentary carbon storage in the Middle Holocene humic lake phase

The development of a humic shallow lake system during the middle Holocene (Lotter 1988) results in high TOC MAR values, between 76 and 730 $g*m^{-2}*yr^{-1}$, supported by a high influx of organic matter, coupled to a high preservation in the seasonally or permanently anoxic water column. The TIC MAR on the other hand decreases with time throughout the early Holocene, with no accumulation of inorganic carbon in the middle Holocene. The disappearance of sedimentary TIC at 6.94 cal ka BP (± 0.19 ka) can be attributed to the development of reducing and low pH conditions in the sediments. Decreased sediment pH values can be related to a high TOC environment (Dean 1999). Based on our data, we suggest that once the organic carbon concentration in the sediments becomes greater than about 15 %, the CO2 produced by decomposition of that OC and production of organic acids lowers the pH of anoxic pore waters enough to dissolve any inorganic carbonates that reaches the sediment-water interface. However, high organic matter content is not enough to lower sedimentary pH, with Swiss sediments generally well-buffered against pH changes (Fiskal et al. 2019). However, a shallow lake would also receive a high contribution of vegetation-derived organic matter, such as humic acids, and as a result have a lower pH not only in the sediments, but throughout the water column. This lake water chemistry, the associated brown water color and the increased amount of shading, would have impacted the amount of primary productivity and the phytoplankton composition (Jasser 1997).

The development of a shallow and organic matter rich lake phase can be coeval with the presence of a seasonally anoxic hypolimnion, as recognized in the increase in Mn and Fe counts (Fig. 2, Supp. Fig. 2). The values of the Mn/Fe ratio are low (≤ 0.15) compared with deep-lake cores from neighboring Lake Zurich (Naeher et al. 2013), which can potentially be explained by the shallow location of the core in the mid-Holocene (0.5-1m depth), leading to less geochemical focusing of the fine-grained Mn and Fe containing minerals. A second potential form for the sedimentary Mn and Fe would be in the form of metal complexes with humic substances (Makri et al. 2021), that are stable in anoxic sediments. A detrital source of Mn and Fe from soils, as described by Makri et al. 2021, is less likely, as the increased values in Mn and Fe are not coeval with increased values in Ti counts (Supp. Fig. 2). A second line of evidence for the development of bottom water anoxia during Unit A2, is a marked increase in both Fe and P counts (300-260 cm blf; 40.7 ± 161 to 3.50 ± 127 a BP), indicating that Fe is potentially present as a PO_4-Fe mineral. These minerals can be formed in anoxic non-sulfidic sediments with high phosphate and Fe^{2+} content (e.g. Lazzaretti et al. 1992). We interpret the presence of increased counts of Fe and P in Rotsee sediments as an indication for persistent anoxic conditions in sediments and bottom water, as these were required to form sedimentary PO_4-Fe in Moossee, a small lake 62 km west of Rotsee (Makri et al. 2021). Inorganic sedimentary composition thus points towards the development of bottom water anoxia and associated high preservation of organic matter as a factor for explaining the high TOC MAR values in the middle Holocene. To test the additional impact of the provenance and type of the organic matter, the molecular and isotopic composition is evaluated.

Macromolecular information shows that early and middle Holocene sediments are characterized by a general increase through time in chlorophyll, lignin and phenol compounds. As lignin is typical for woody tissues in wood and bark, and phenols and chlorophyll also present in plant tissues, this implies increasing contribution of woody vegetation to the lake sediments. Maximum values are observed at 6.5 cal ka BP (Fig. 4). This timing matches very well with the onset of the shallow humic lake phase at 6.94 cal ka BP (± 0.19 ka). To determine changes in contribution of all vascular plant matter, the concentration of aDNA from Eukaryote and Tracheophyta (vascular plants) is evaluated (Fig. 3F; Fig. 4). While both vascular plants and lignin are present throughout the early and middle Holocene, the highest value (n=1) is observed during the proposed shallow humic lake phase. In addition to the development of an anoxic lake system, the organic matter supplied to the lake system was derived from vegetation, rich in lignin and therefore more recalcitrant (Martínez et al. 2005), contributing to the high MAR values in middle Holocene sediments.

In Rotsee, successional changes in lake water depth, chemistry (pH and hypolimnion ventilation), and organic matter provenance result in a large change in the type of sedimentary organic matter. While the individual effects of these drivers cannot be distinguished, it is clear that millennial-scale successional changes, specifically lake infilling, promote the storage of sedimentary organic carbon.

Human land use changes and climate impact Late Holocene Rotsee sediments

Impact of successional and land use changes

Without environmental changes, the shallow lake phase is generally the last successional stage (Johnson and Miyanishi 2008 and references therein) before a lake gets filled in. A deepening of a shallow lake system can be caused by an increase in precipitation or a decrease in evaporation, increasing the lake water balance. During the late Holocene, after 6 ka B.P, decreasing solar insolation values caused the establishment of the modern atmospheric circulation pattern, with stronger westerly winds. The increase in precipitation and wind impact (Niessen and Kelts 1989) in Switzerland may have impacted both the lake level and mixing intensity of Rotsee. Indeed, a gradual change in organic carbon composition, as reflected by a decrease in the contribution of vascular macromolecules (phenols) and aDNA starts between 4.6 and 6.5 cal ka BP (Fig. 4), indicating that the contribution of shoreline forest to the sediments was decreased. This was not associated with an increase in larger grain sizes (Ti/Al; Fig. 2), indicating that the loss of the Rotsee shoreline vegetation did not cause extensive soil erosion. The impact of prehistoric land use changes, which are described from the wider region to occur from 5 cal ka BP on (Lotter 1988), is not recognized in Rotsee sediments.

There is however a substantial temporal offset between the establishment of the modern atmospheric circulation pattern and recovery from permanently anoxic conditions at 3.5 ± 0.1 cal ka BP, based on decreasing sedimentary P and Mn content of the sediments, (P/Ti and Mn/Fe, Fig. 2). This change was coeval with an increase in $\delta^{15}N_{-TN}$ and included distinct phases with increased soil erosion and water column ventilation, as indicated by peaks in Ti/Al values (onset dated at 3.1 ± 0.2, 2.7 ± 0.2 and 1.8 ± 0.2) and low Mn/Fe ratio values. We therefore follow the hypothesis that land use changes strongly impacted the Rotsee watershed (forest felling) impacted the Rotsee sediments in the Late Holocene. The latest, largest event co-occurs with known episodes of large forest cover removal during Roman times, while the earlier two events can be interpreted as smaller deforestation events. Interestingly, high TOC MARs (650 $g*m^{-2}*yr^{-1}$) are reconstructed for Roman times. This deforestation period likely increased nutrient input from the watershed, as inferred from sedimentary $\delta^{15}N_{-TN}$. The Ti/Al ratio shows two additional episodes of increased soil erosion during the Middle Ages (maxima at 644 ± 220 and 1175 to 1255 ± 210 AD), and then again in recent sediments (1949 ± 9 AD and 1961 ± 2 AD). These events are generally not co-eval with periods of high sedimentary C storage (Fig. 3B). The impact of land use changes and the associated recovery from the reducing conditions that started 3.6 ± 0.1 ka BP had a delayed but significant impact on the inorganic carbon MAR. The recovery from the shallow water phase resulted in the preservation and observed increase in TIC in the top 111 cm of the lake core (908 ± 223 cal a BP). The hypothesis that land use changes determine the sedimentary carbon storage in late Holocene sediments is thus supported.

The impact of recent eutrophication on sedimentary carbon in the last 150 year

Current MAR in the deepest anoxic sediments of Rotsee (MAR= 172 gC * m^{-2} * yr^{-1}; Steinsberger et al. 2017), are high compared with a diversity of Swiss lakes, reflecting the mesotrophic state of the lake (Steinsberger et al. 2017). At the location of the core, MAR peaks at 300 gC*m^{-2}*yr^{-1} between 1950 and 1970 AD, corresponding with the maximum eutrophication in the 1970s (Fiskal et al. 2019). These values greatly exceed the current MAR in Rotsee anoxic sediments. In the top 2-10 cm, TOC MAR varies between 30-50 gC *m^{-2}*yr^{-1}, which is lower than the reported TOC MAR in the anoxic sediments (Steinsberger et al. 2017). These offsets can be attributed to the core location, which is currently outside of the extent of the seasonally anoxic water column. During the 1970 eutrophication period, the oxycline was expected to be shallower, and extended bottom water anoxia is a factor to explain the change in MAR during the last 150 years. In addition, changes in MAR could be attributed to either the amount of primary productivity, or the recalcitrance of the organic matter. The surface sediments contain a large fraction of organic matter (esters, fatty acids) that are generally not conserved over long timescales, whose decrease in fractional abundance primarily reflects degradation. In contrast, N-containing compounds reach maximum values (17-19 %) 85 to 100 years ago (12 to 28 ± 13 to 96 cal a BP; 1938 to 1922 AD), coeval with an increase in Chlorophyta aDNA at 12 ± 13 cal a BP (1938 AD). This is interpreted as an increase in primary productivity coeval with either an initial phase of anthropogenic eutrophication in Rotsee (Lotter 1989), or the trophic increase caused by the establishment of the Reuss canal in 1922. Diatom DNA only increases slightly later, from 1943 AD ± 11. The impact of anthropogenic eutrophication on lake primary productivity has thus impacted the composition of subsurface macromolecular composition. Although this has resulted in the subsurface MARs maximum, the amount of organic and inorganic matter accumulated was minor compared to the middle Holocene and early Holocene, respectively. Extensive eutrophication in the current cultural landscape thus does not result in the highest MARs of the Holocene at the coring location.

Conclusion

The sedimentary carbon stored in Rotsee responds to climate-driven successional changes, from an oligotrophic macrophyte-dominated system and low carbon storage, to a phytoplankton dominated system with substantial inorganic carbon stored, to a humic shallow lake system dominated by organic sedimentary carbon. In the Late Holocene, increasing nutrient inputs, following deforestation or human eutrophication, drives organic carbon accumulation rates. Changes in temperature, succession, lake water chemistry and redox conditions have a compound effect on the type and amount of sedimentary carbon. The largest changes observed, from late glacial to Holocene, indicate that current climate change is most likely to impact lakes that are currently in an oligotrophic macrophyte-dominated stage. The natural filling in of lakes results in high concentrations of organic carbon stored, while inorganic carbon is not stored efficiently in these systems. From a long-term carbon storage perspective, unmanaged lake systems thus show a clear temporal difference in the type of carbon stored. However, although the type of carbon changes with time, there is no long-term trend in the amount of carbon stored in Rotsee sediments over the Holocene time period.

Acknowledgments

The authors acknowledge the following colleagues for contribution to organization of fieldwork and subsampling: Clemens Glombitza, Adrian Gilli, Anita Schlatter, Pascal Rünzi, Linn Speidel, Benedict Mittelbach, Fatemeh Ajallooeian; for performing laboratory work extracting aDNA in the framework of a BSc and MSc thesis: Tabea Patt and Sarah Wolf; for preparing samples for analysis (freeze-drying and grinding), as well as performing bulk C and N amount and isotopes: Serge Robert and Irene Brunner. CDJ acknowledges SNSF PRIMA fellowship funding Grant number 179783.

References (60)

Affolter S, Häuselmann A, Fleitmann D, et al (2019) Central Europe temperature constrained by speleothem fluid inclusion water isotopes over the past 14,000 years. Science Advances 5: eaav3809

Ammann B (1986) Litho- and palynostratigraphy at Lobsigensee: Evidences for trophic changes during the Holocene. Hydrobiologia 143: 301–307

Anderson NJ, Bennion H, Lotter AF (2014) Lake eutrophication and its implications for organic carbon sequestration in Europe. Global Change Biology 20: 2741–2751

Avnimelech Y, Ritvo G, Meijer LE, Kochba M (2001) Water content, organic carbon and dry bulk density in flooded sediments. Aquacultural Engineering 25: 25–33

Bader RG (1957) The lignin fraction of marine sediments. Deep Sea Research (1953) 4: 15–22

Baud A, Smol JP, Meyer-Jacob C, et al (2023) The impacts of whole-lake acidification and eutrophication on the accumulation of lead in sediments from manipulated lakes in the Experimental Lakes Area (IISD-ELA). Environmental Pollution 317: 120829

Blaauw M, Christen JA (2011) Flexible paleoclimate age-depth models using an autoregressive gamma process. Bayesian Analysis 6: 457–474

Brady NC, Weil RR (2016) The nature and properties of soils, Fifteenth edition, global edition. Pearson, Harlow, England London New York

Davison W (1993) Iron and manganese in lakes. Earth-Science Reviews 34: 119–163

Dean WE (1999) The carbon cycle and biogeochemical dynamics in lake sediments. Journal of Paleolimnology 21: 375–393

Deng L, Bölsterli D, Kristensen E, et al (2020) Macrofaunal control of microbial community structure in continental margin sediments. Proceedings of the National Academy of Sciences 117: 15911–15922

Fiskal A, Deng L, Michel A, et al (2019) Effects of eutrophication on sedimentary organic carbon cycling in five temperate lakes. Biogeosciences 16: 3725–3746

Gajendra N, Berg JS, Vogel H, et al (2023) Carbohydrate compositional trends throughout Holocene sediments of an alpine lake (Lake Cadagno). Frontiers in Earth Science 11: 1047224

Gudasz C, Bastviken D, Steger K, et al (2010) Temperature-controlled organic carbon mineralization in lake sediments. Nature 466:478–481.

Haas M, Baumann F, Castella D, et al (2019) Roman-driven cultural eutrophication of Lake Murten, Switzerland. Earth and Planetary Science Letters 505: 110–117.

Han X, Tolu J, Deng L, et al (2022) Long-term preservation of biomolecules in lake sediments: potential importance of physical shielding by recalcitrant cell walls. PNAS Nexus 1:pgac076

Hasler AD (1947) Eutrophication of Lakes by Domestic Drainage. Ecology 28: 383–395.

Heiri O, Lotter AF (2003) 9000 years of chironomid assemblage dynamics in an Alpine lake: long-term trends, sensitivity to disturbance, and resilience of the fauna. Journal of Paleolimnology 30:273–289

Hofmann A, Roussy D, Filella M (2002) Dissolved silica budget in the North basin of Lake Lugano. Chemical Geology 182: 35–55

Höhn L, Leunda M, Gobet E, et al (2022) Vegetation response to rapid climate change during the Lateglacial–Early Holocene transition at Gola di Lago, southern Switzerland. Boreas 51: 606–620

Jasser I (1997) The dynamics and importance of picoplankton in shallow, dystrophic lake in comparison with surface waters of two deep lakes with contrasting trophic status. Hydrobiologia 342: 87–93

Johnson EA, Miyanishi K (2008) Testing the assumptions of chronosequences in succession. Ecology Letters 11: 419–431

Jones BF, Bowser CJ (1978) The Mineralogy and Related Chemistry of Lake Sediments. In: Lerman A (ed) Lakes. Springer New York, New York, NY, pp 179–235

Kastowski M, Hinderer M, Vecsei A (2011) Long-term carbon burial in European lakes: Analysis and estimate. Global Biogeochemical Cycles 25 (3): GB3019

Lazzaretti MA, Hanselmann KW, Brandl H, et al (1992) The role of sediments in the phosphorus cycle in Lake Lugano. II. Seasonal and spatial variability of microbiological processes at the sediment-water interface. Aquatic Science 54: 285–299

Lever MA, Torti A, Eickenbusch P, et al (2015) A modular method for the extraction of DNA and RNA, and the separation of DNA pools from diverse environmental sample types. Frontiers in Microbiology 6: 476

Lim J, Lee J-Y, Hong S-S, et al (2019) Holocene coastal environmental change and ENSO-driven hydroclimatic variability in East Asia. Quaternary Science Reviews 220: 75–86

Liu X, Colman SM, Brown ET, et al (2013) Estimation of carbonate, total organic carbon, and biogenic silica content by FTIR and XRF techniques in lacustrine sediments. J Paleolimnol 50: 387–398

Lotter AF, Birks HJB, Eicher U, et al (2000) Younger Dryas and Allerød summer temperatures at Gerzensee (Switzerland) inferred from fossil pollen and cladoceran assemblages. Palaeogeography, Palaeoclimatology, Palaeoecology 159: 349–361.

Lotter AF (1988) Paläoökologische und paläolimnologische Studie des Rotsees bei Luzern. Dissertationes Botanicae, Band 124. Publisher: Schweizerbart Science Publishers, Germany.

Lotter AF (1989) Subfossil and modern diatom plankton and the paleolimnology of Rotsee (Switzerland) since 1850. Aquatic Science 51: 338–350

Makri S, Wienhues G, Bigalke M, et al (2021) Variations of sedimentary Fe and Mn fractions under changing lake mixing regimes, oxygenation and land surface processes during Late-glacial and Holocene times. Science of The Total Environment 755: 143418

Marchand L, Mench M, Jacob DL, Otte ML (2010) Metal and metalloid removal in constructed wetlands, with emphasis on the importance of plants and standardized measurements: A review. Environmental Pollution 158: 3447–3461

Martínez AT, Speranza M, Ruiz-Dueñas FJ, et al (2005) Biodegradation of lignocellulosics: microbial, chemical, and enzymatic aspects of the fungal attack of lignin. Int Microbiol 8:195–204

Meyers S (2014) astrochron: A Computational Tool for Astrochronology. 1.4

Moscariello A, Schneider AM, Filippi ML (1998) Late glacial and early Holocene palaeoenvironmental changes in Geneva Bay (Lake Geneva, Switzerland). Palaeogeography, Palaeoclimatology, Palaeoecology 140: 51–73

Moser KA, Baron JS, Brahney J, et al (2019) Mountain lakes: Eyes on global environmental change. Global and Planetary Change 178: 77–95

Naeher S, Gilli A, North RP, et al (2013) Tracing bottom water oxygenation with sedimentary Mn/Fe ratios in Lake Zurich, Switzerland. Chemical Geology 352: 125–133

Nicolussi K, Kaufmann M, Patzelt G, et al (2005) Holocene tree-line variability in the Kauner Valley, Central Eastern Alps, indicated by dendrochronological analysis of living trees and subfossil logs. Veget Hist Archaeobot 14: 221–234

Niessen F, Kelts K (1989) The deglaciation and Holocene sedimentary evolution of southern perialpine Lake Lugano: implications for Alpine paleoclimate. Eclogae Geol Helv 82: 235–263

Ninnes S, Tolu J, Meyer-Jacob C, et al (2017) Investigating molecular changes in organic matter composition in two Holocene lake-sediment records from central Sweden using pyrolysis-GC/MS. JGR Biogeosciences 122: 1423–1438

Norris MW, Turnbull JC, Howarth JD, Vandergoes MJ (2020) Pretreatment of Terrestrial Macrofossils. Radiocarbon 62: 349–360

Olsen J, Björck S, Leng MJ, et al (2010) Lacustrine evidence of Holocene environmental change from three Faroese lakes: a multiproxy XRF and stable isotope study. Quaternary Science Reviews 29: 2764–2780

Pastorino P, Elia AC, Pizzul E, et al (2024) The old and the new on threats to high-mountain lakes in the Alps: A comprehensive examination with future research directions. Ecological Indicators 160:

111812

Reber R, Akçar N, Ivy-Ochs S, et al (2014) Timing of retreat of the Reuss Glacier (Switzerland) at the end of the Last Glacial Maximum. Swiss J Geosci 107: 293–307

Reimer PJ, Austin WEN, Bard E, et al (2020) The IntCal20 Northern Hemisphere Radiocarbon Age Calibration Curve (0–55 cal kBP). Radiocarbon 62: 725–757

Renssen H, Seppä H, Crosta X, et al (2012) Global characterization of the Holocene Thermal Maximum. Quaternary Science Reviews 48: 7–19

Samartin S, Heiri O, Vescovi E, et al (2012) Lateglacial and early Holocene summer temperatures in the southern Swiss Alps reconstructed using fossil chironomids. Journal of Quaternary Science 27:279–289

Steinsberger T, Schmid M, Wüest A, et al (2017) Organic carbon mass accumulation rate regulates the flux of reduced substances from the sediments of deep lakes. Biogeosciences 14:3275–3285

Teranes JL, Bernasconi SM (2000) The record of nitrate utilization and productivity limitation provided by δ^{15}N values in lake organic matter—A study of sediment trap and core sediments from Baldeggersee, Switzerland. Limnology and Oceanography 45: 801–813

Tolu J, Gerber L, Boily J-F, Bindler R (2015) High-throughput characterization of sediment organic matter by pyrolysis–gas chromatography/mass spectrometry and multivariate curve resolution: A promising analytical tool in (paleo)limnology. Analytica Chimica Acta 880: 93–102

Trautmann S, Knoflach B, Stötter J, et al (2023) Potential impacts of a changing cryosphere on soils of the European Alps: A review. CATENA 232: 107439

Ursenbacher S, Stötter T, Heiri O (2020) Chitinous aquatic invertebrate assemblages in Quaternary lake sediments as indicators of past deepwater oxygen concentration. Quaternary Science Reviews 231: 106203

Verbruggen F, Heiri O, Reichart G-J, Lotter AF (2010) Chironomid δ^{18}O as a proxy for past lake water δ^{18}O: a Lateglacial record from Rotsee (Switzerland). Quaternary Science Reviews 29: 2271–2279

Vollweiler N, Scholz D, Mühlinghaus C, et al (2006) A precisely dated climate record for the last 9 kyr from three high alpine stalagmites, Spannagel Cave, Austria. Geophysical Research Letters 33 (20): L20703

Welten M (1982) Vegetationsgeschichtliche Untersuchung in den westlichen schweizer Alpen. Bern - Wallis. Published by Birkhauser, Boston (USA).

Wick L, Tinner W (1997) Vegetation Changes and Timberline Fluctuations in the Central Alps as Indicators of Holocene Climatic Oscillations. Arctic and Alpine Research 29: 445–458

Willerslev E, Hansen AJ, Binladen J, et al (2003) Diverse Plant and Animal Genetic Records from Holocene and Pleistocene Sediments. Science 300: 791–795

Zhao Y, Liu Z, Colin C, et al (2011) Turbidite deposition in the southern South China Sea during the last glacial: Evidence from grain-size and major elements records. Chin Sci Bull 56: 3558–3565

Züllig H, Rheineck S (1985) Pigmente phototropher Bakterien in Seesedimenten und ihre Bedeutung für die Seenforschung. Schweiz Z Hydrol 47: 87–126

Captions

Fig.1. Visual overview of the Lake Rotsee core with (A) a photographic image of the sedimentary units, with an asterisk indicating a change in picture exposure impacting image lightness within Unit A3. The proposed age model plotted is based on 19 ^{14}C dated macrofossils and unsupported ^{210}Pb measurements (inset). The depth range of ^{14}C ages that is based on macrophyte macrofossils is indicated in a red rectangle, and depth and age intervals of core sections are tabulated. Also inset are the summary of rplum model parameters. Panel B reports the estimated sedimentation rates ($_{10}$log(mm * yr^{-1})), where the black line indicates the sedimentation rate at a cm resolution and the red line depicts the smoothed trends.

Fig. 2. Overview of main Rotsee parameters plotted against composite depth (cm below lake floor (blf)); sedimentary content (%) of total inorganic carbon (TIC) and total carbon (TIC + total organic carbon (TOC)), the values of the first two principal components of the XRF variability (XRF PC1, XRF PC2) with percentage of variance explained indicated, XRF based ratios Ti/Al, Ca/Ti, Si/Ti, Mn/Fe, Fe/Ti, P/Ti. Parameters are plotted grouped per sedimentary parameter (carbon (C) composition, clastic material, lake productivity, and redox indicators.

Fig. 3. Change of A) sedimentation rate ($_{10}$log mm*yr^{-1}), B) mass accumulation rates (MAR) of sedimentary total inorganic carbon (TIC) and total carbon (TIC + total organic carbon (TOC)), C) TOC/TN (TOC / total nitrogen), D) bulk $\delta^{13}C_{\text{-TOC}}$, E) bulk $\delta^{15}N_{\text{-TN}}$ and rbcL and F) 18S rRNA gene copy (gene count * g sed $^{-1}$) with time. Younger Dryas is indicated in green, Holocene warm periods are indicated in yellow. The most recent 100 years are replotted on a more detailed scale.

Fig. 4. In comparison with the sedimentary content (%) of total inorganic carbon (TIC) and total carbon (TIC + total organic carbon) (for higher resolution, see Fig. 2), the distribution of organic compound classes in Rotsee sediments is plotted (Supp. Table 2 for composition of compound classes), with the carbohydrate composition replotted on a separate scale. The relative abundance of aDNA of Tracheophyta, Chlorophyta and Ochrophyta rbcL gene copies compared to the Eukaryotic 18S rRNA gene copies are plotted. Background color of the tabulated ages and depths indicate Holocene climate zones, with Younger Dryas indicated in green and Holocene warm periods are indicated in yellow.

Figures

Fig. 1

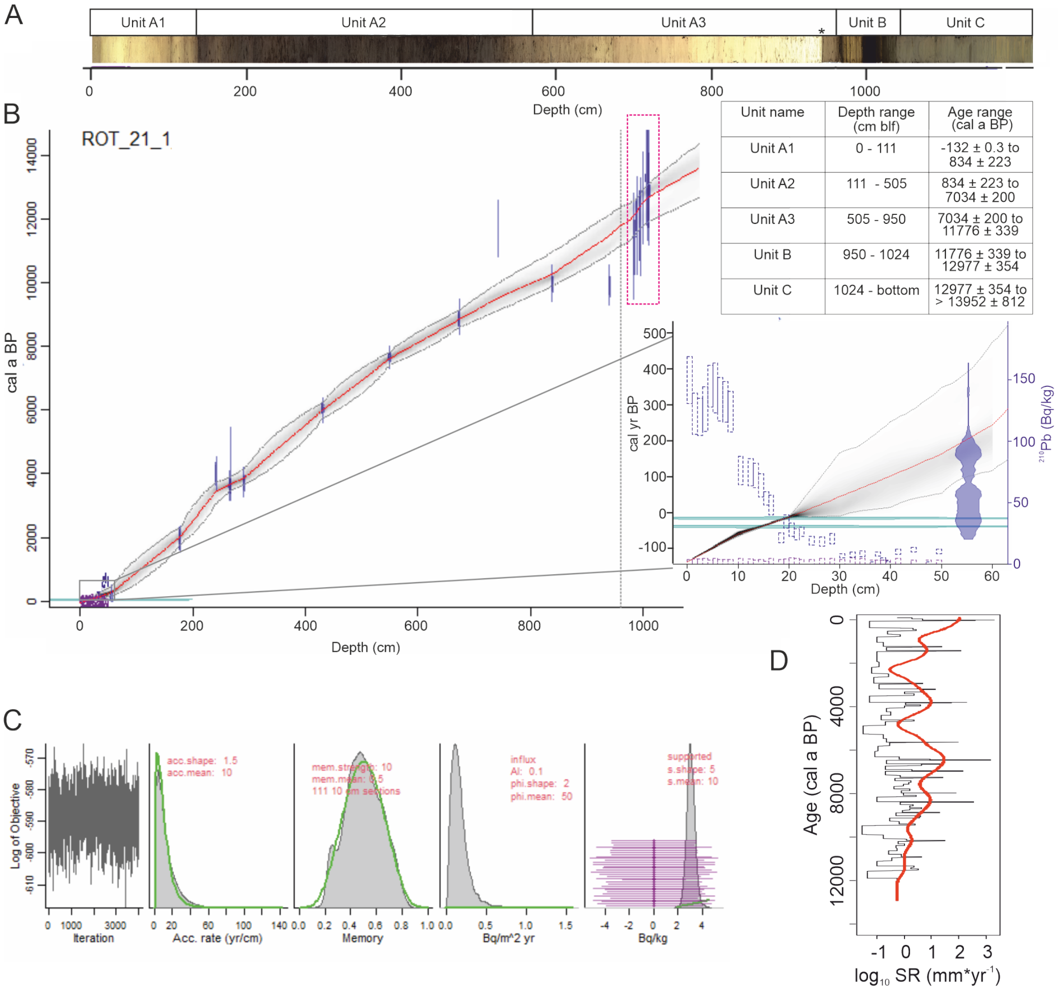

Unit name	Depth range (cm blf)	Age range (cal a BP)
Unit A1	0 - 111	-132 ± 0.3 to 834 ± 223
Unit A2	111 - 505	834 ± 223 to 7034 ± 200
Unit A3	505 - 950	7034 ± 200 to 11776 ± 339
Unit B	950 - 1024	11776 ± 339 to 12977 ± 354
Unit C	1024 - bottom	12977 ± 354 to > 13952 ± 812

Fig. 2

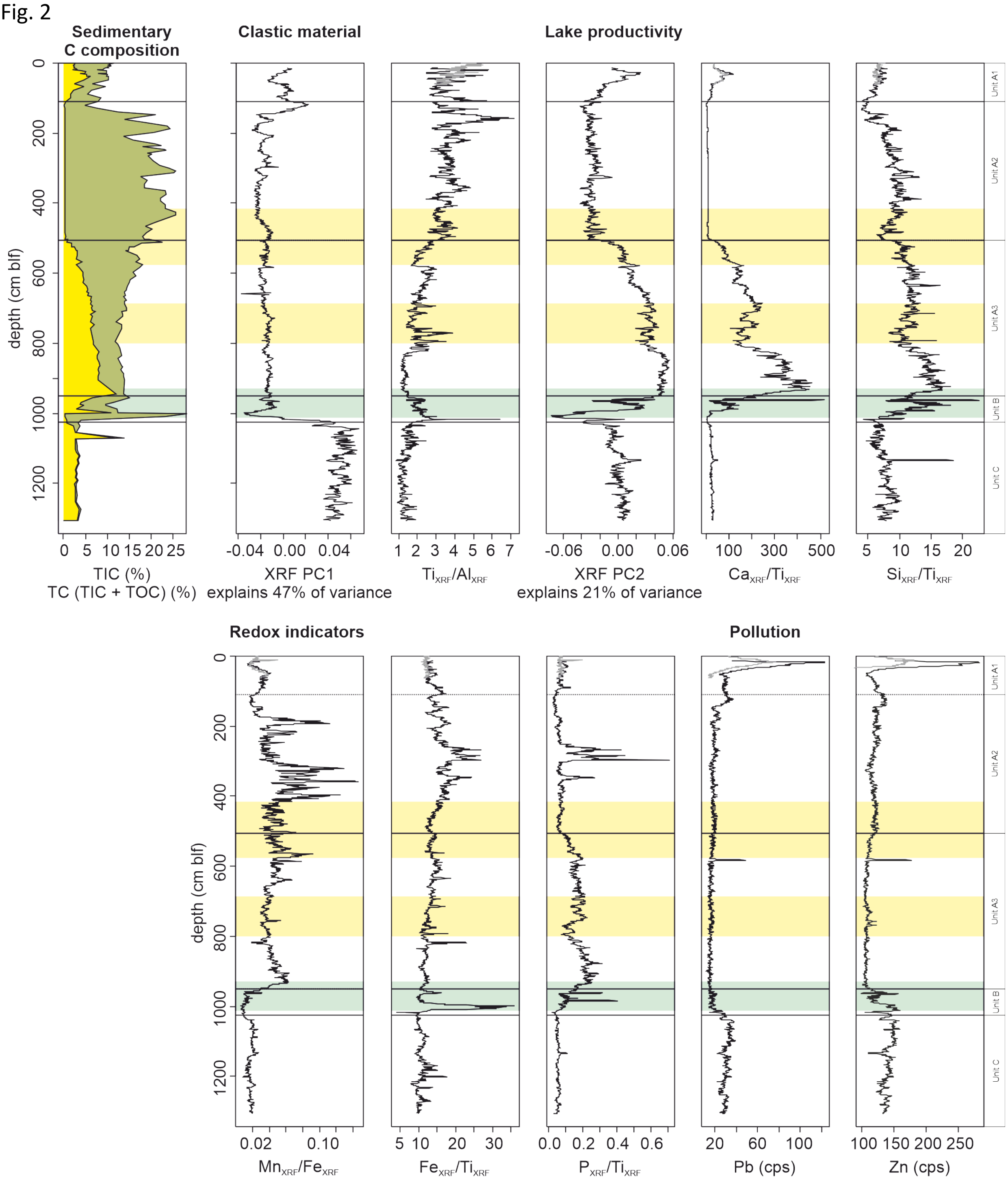
Sedimentary C composition
Clastic material
Lake productivity
depth (cm blf)
0
200
400
600
800
1000
1200
0 5 10 15 20 25
TIC (%)
TC (TIC + TOC) (%)
-0.04 0.00 0.04
XRF PC1
explains 47% of variance
1 2 3 4 5 6 7
Ti_XRF/Al_XRF
-0.06 0.00 0.06
XRF PC2
explains 21% of variance
100 300 500
Ca_XRF/Ti_XRF
5 10 15 20
Si_XRF/Ti_XRF
Unit A1
Unit A2
Unit A3
Unit B
Unit C
Redox indicators
Pollution
0.02 0.10
Mn_XRF/Fe_XRF
5 10 20 30
Fe_XRF/Ti_XRF
0.0 0.2 0.4 0.6
P_XRF/Ti_XRF
20 60 100
Pb (cps)
100 150 200 250
Zn (cps)

Fig. 3

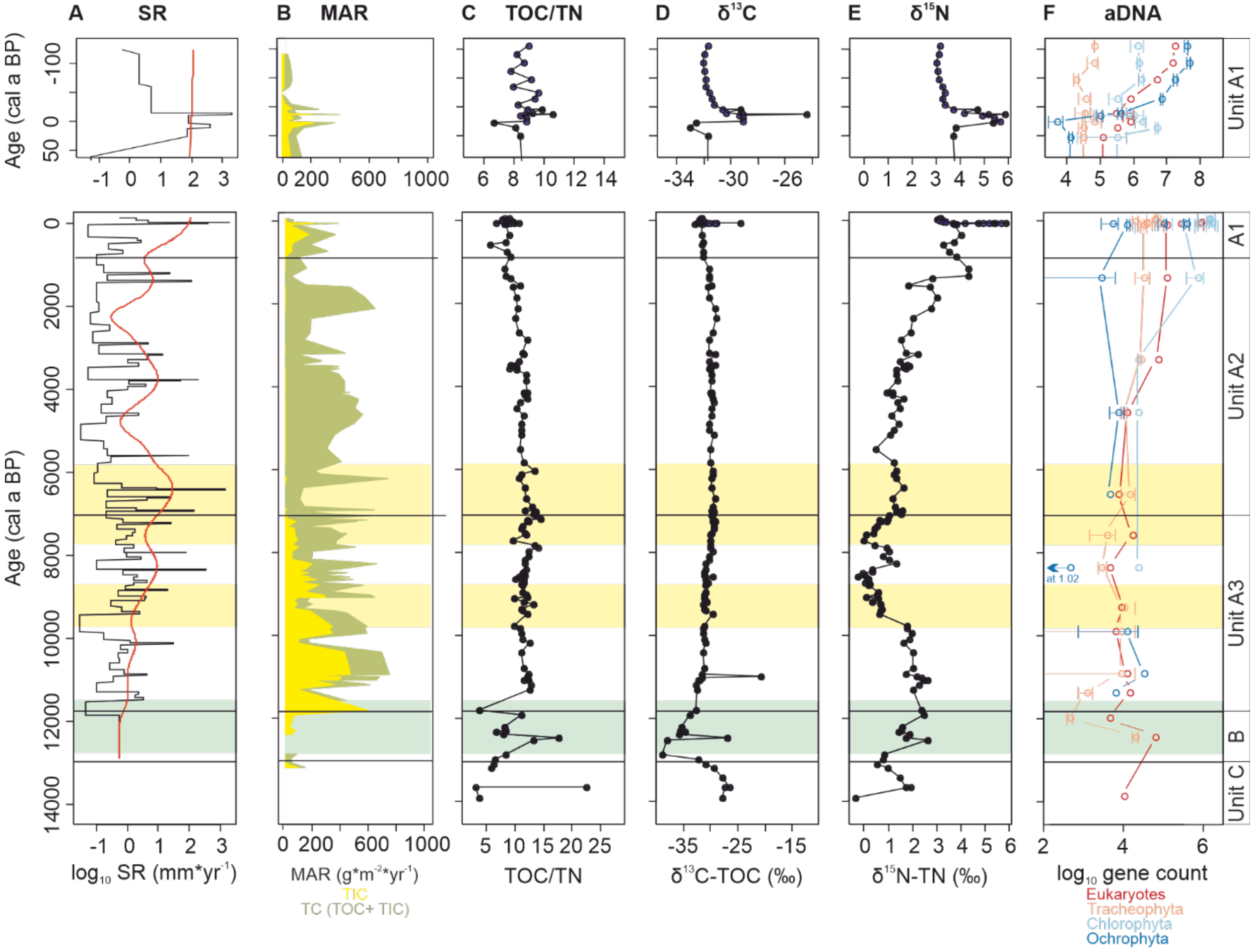
A SR
B MAR
C TOC/TN
D δ13C
E δ15N
F aDNA
Age (cal a BP)
-100
0
50
-1 0 1 2 3
0 200 600 1000
6 8 10 12 14
-34 -30 -26
0 1 2 3 4 5 6
4 5 6 7 8
Unit A1
0
2000
4000
6000
8000
10000
12000
14000
log10 SR (mm*yr-1)
MAR (g*m-2*yr-1)
TIC
TC (TOC+ TIC)
5 10 15 20 25
TOC/TN
-35 -25 -15
δ13C-TOC (‰)
δ15N-TN (‰)
2 4 6
log10 gene count
Eukaryotes
Tracheophyta
Chlorophyta
Ochrophyta
at 1.02
A1
Unit A2
Unit A3
B
Unit C

Fig. 4

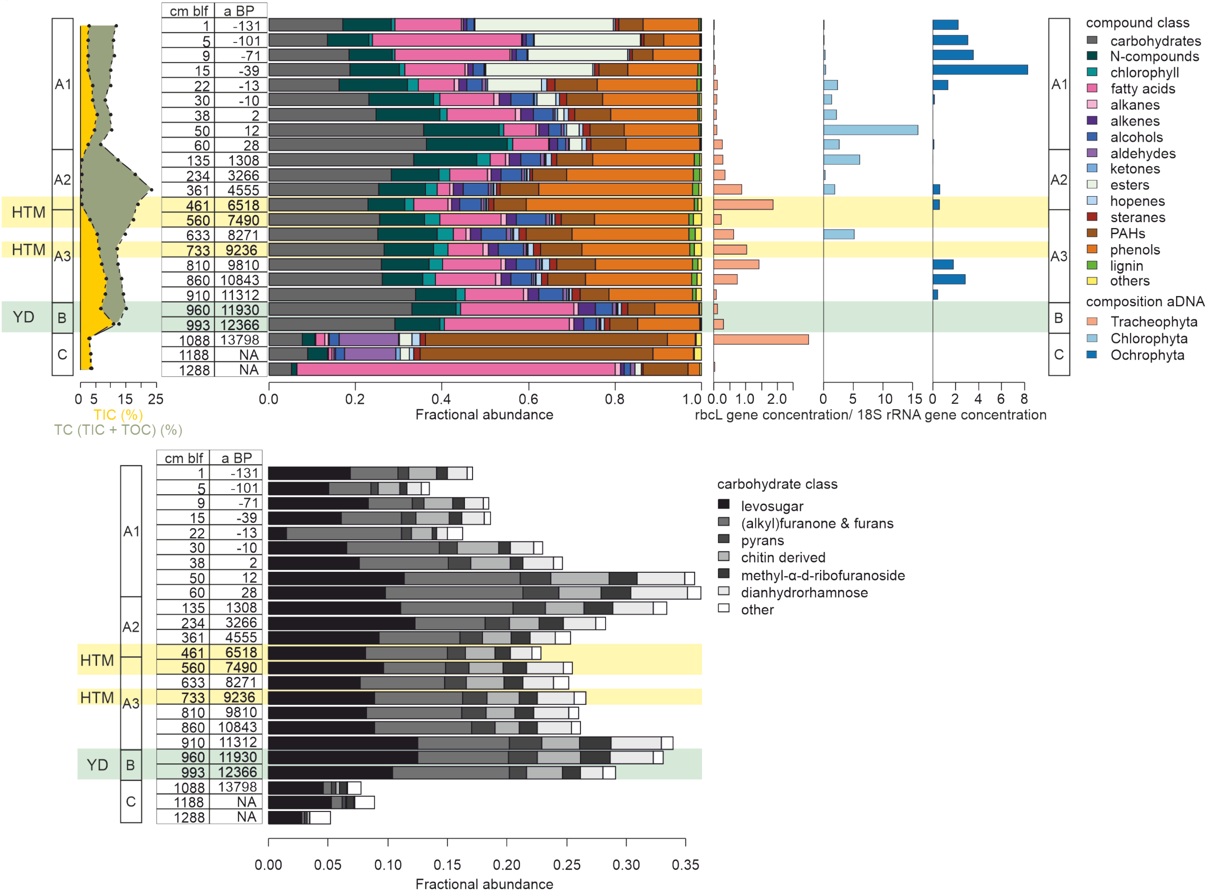
cm blf
a BP
1 -131
5 -101
9 -71
15 -39
22 -13
30 -10
38 2
50 12
60 28
135 1308
234 3266
361 4555
461 6518
560 7490
633 8271
733 9236
810 9810
860 10843
910 11312
960 11930
993 12366
1088 13798
1188 NA
1288 NA
A1
A2
A3
B
C
HTM
HTM
YD
0 5 15 25
TIC (%)
TC (TIC + TOC) (%)
0.0 0.2 0.4 0.6 0.8 1.0
Fractional abundance
0.0 1.0 2.0
0 5 10 15
0 2 4 6 8
rbcL gene concentration/ 18S rRNA gene concentration
compound class
carbohydrates
N-compounds
chlorophyll
fatty acids
alkanes
alkenes
alcohols
aldehydes
ketones
esters
hopenes
steranes
PAHs
phenols
lignin
others
composition aDNA
Tracheophyta
Chlorophyta
Ochrophyta
carbohydrate class
levosugar
(alkyl)furanone & furans
pyrans
chitin derived
methyl-α-d-ribofuranoside
dianhydrorhamnose
other
0.00 0.05 0.10 0.15 0.20 0.25 0.30 0.35
Fractional abundance

Supplementary Materials to the manuscript:

Holocene environmental change in Rotsee, and its impact on sedimentary carbon storage

Cindy De Jonge[1], Nathalie Dubois[2], Nemiah Ladd[3], Longhui Deng [4], Niroshan Gajendra [4,5], Negar Haghipour [1, 6], Carsten J. Schubert[4, 7], Mark Lever[4, 8]

[1] Geological Institute, ETH Zurich, Sonneggstrasse 5, 8092 Zurich, Switzerland

[2] Department of Surface Waters Research and Management, Eawag, Uberlandstrasse 133, 8600 Dubendorf, Switzerland.

[3] Department of Environmental Sciences, University of Basel, Bernoullistrasse 30/32, 4056 Basel, Switzerland

[4] Institute of Biogeochemistry and Pollutant Dynamics, ETH Zurich, Universitaetstrasse 16, Zurich, Switzerland

[5] Currently at: Institute for Energy Technology (IFE), Instituttveien 18, 2007, Kjeller, Norway

[6] Laboratory of Ion Beam Physics, ETH Zurich, Switzerland.

[7] Department of Surface Waters, EAWAG, Swiss Federal Institute of Aquatic Science and Technology, Kastanienbaum, Switzerland.

[8] Currently at: Marine Science Institute, University of Texas at Austin, 750 Channel View Drive, Port Aransas, TX 78373, USA.

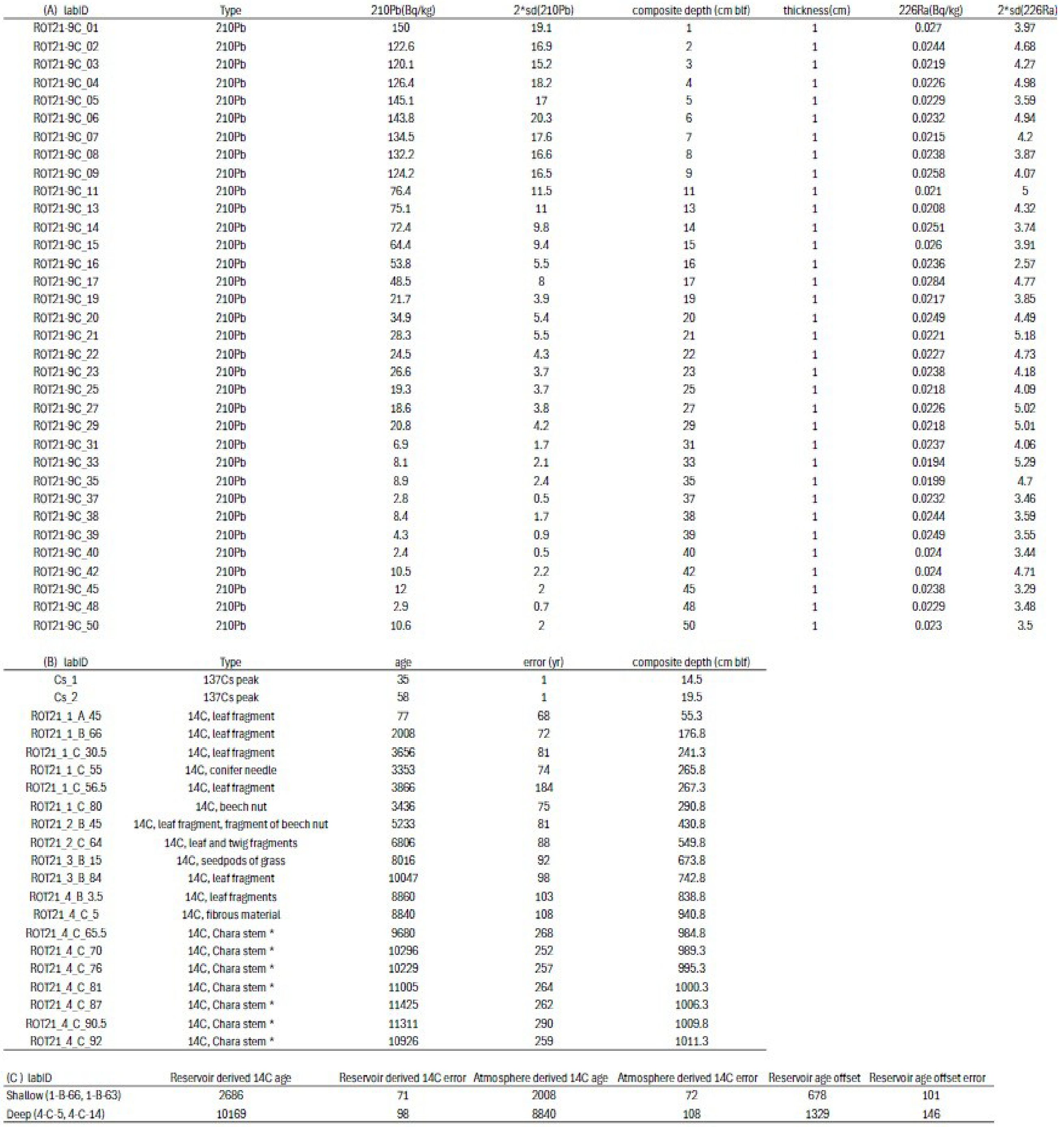

(A) labID	Type	210Pb(Bq/kg)	2*sd(210Pb)	composite depth (cm blf)	thickness(cm)	226Ra(Bq/kg)	2*sd(226Ra)
ROT21-9C_01	210Pb	150	19.1	1	1	0.027	3.97
ROT21-9C_02	210Pb	122.6	16.9	2	1	0.0244	4.68
ROT21-9C_03	210Pb	120.1	15.2	3	1	0.0219	4.27
ROT21-9C_04	210Pb	126.4	18.2	4	1	0.0226	4.98
ROT21-9C_05	210Pb	145.1	17	5	1	0.0229	3.59
ROT21-9C_06	210Pb	143.8	20.3	6	1	0.0232	4.94
ROT21-9C_07	210Pb	134.5	17.6	7	1	0.0215	4.2
ROT21-9C_08	210Pb	132.2	16.6	8	1	0.0238	3.87
ROT21-9C_09	210Pb	124.2	16.5	9	1	0.0258	4.07
ROT21-9C_11	210Pb	76.4	11.5	11	1	0.021	5
ROT21-9C_13	210Pb	75.1	11	13	1	0.0208	4.32
ROT21-9C_14	210Pb	72.4	9.8	14	1	0.0251	3.74
ROT21-9C_15	210Pb	64.4	9.4	15	1	0.026	3.91
ROT21-9C_16	210Pb	53.8	5.5	16	1	0.0236	2.57
ROT21-9C_17	210Pb	48.5	8	17	1	0.0284	4.77
ROT21-9C_19	210Pb	21.7	3.9	19	1	0.0217	3.85
ROT21-9C_20	210Pb	34.9	5.4	20	1	0.0249	4.49
ROT21-9C_21	210Pb	28.3	5.5	21	1	0.0221	5.18
ROT21-9C_22	210Pb	24.5	4.3	22	1	0.0227	4.73
ROT21-9C_23	210Pb	26.6	3.7	23	1	0.0238	4.18
ROT21-9C_25	210Pb	19.3	3.7	25	1	0.0218	4.09
ROT21-9C_27	210Pb	18.6	3.8	27	1	0.0226	5.02
ROT21-9C_29	210Pb	20.8	4.2	29	1	0.0218	5.01
ROT21-9C_31	210Pb	6.9	1.7	31	1	0.0237	4.06
ROT21-9C_33	210Pb	8.1	2.1	33	1	0.0194	5.29
ROT21-9C_35	210Pb	8.9	2.4	35	1	0.0199	4.7
ROT21-9C_37	210Pb	2.8	0.5	37	1	0.0232	3.46
ROT21-9C_38	210Pb	8.4	1.7	38	1	0.0244	3.59
ROT21-9C_39	210Pb	4.3	0.9	39	1	0.0249	3.55
ROT21-9C_40	210Pb	2.4	0.5	40	1	0.024	3.44
ROT21-9C_42	210Pb	10.5	2.2	42	1	0.024	4.71
ROT21-9C_45	210Pb	12	2	45	1	0.0238	3.29
ROT21-9C_48	210Pb	2.9	0.7	48	1	0.0229	3.48
ROT21-9C_50	210Pb	10.6	2	50	1	0.023	3.5

(B) labID	Type	age	error (yr)	composite depth (cm blf)
Cs_1	137Cs peak	35	1	14.5
Cs_2	137Cs peak	58	1	19.5
ROT21_1_A_45	14C, leaf fragment	77	68	55.3
ROT21_1_B_66	14C, leaf fragment	2008	72	176.8
ROT21_1_C_30.5	14C, leaf fragment	3656	81	241.3
ROT21_1_C_55	14C, conifer needle	3353	74	265.8
ROT21_1_C_56.5	14C, leaf fragment	3866	184	267.3
ROT21_1_C_80	14C, beech nut	3436	75	290.8
ROT21_2_B_45	14C, leaf fragment, fragment of beech nut	5233	81	430.8
ROT21_2_C_64	14C, leaf and twig fragments	6806	88	549.8
ROT21_3_B_15	14C, seedpods of grass	8016	92	673.8
ROT21_3_B_84	14C, leaf fragment	10047	98	742.8
ROT21_4_B_3.5	14C, leaf fragments	8860	103	838.8
ROT21_4_C_5	14C, fibrous material	8840	108	940.8
ROT21_4_C_65.5	14C, Chara stem *	9680	268	984.8
ROT21_4_C_70	14C, Chara stem *	10296	252	989.3
ROT21_4_C_76	14C, Chara stem *	10229	257	995.3
ROT21_4_C_81	14C, Chara stem *	11005	264	1000.3
ROT21_4_C_87	14C, Chara stem *	11425	262	1006.3
ROT21_4_C_90.5	14C, Chara stem *	11311	290	1009.8
ROT21_4_C_92	14C, Chara stem *	10926	259	1011.3

(C) labID	Reservoir derived 14C age	Reservoir derived 14C error	Atmosphere derived 14C age	Atmosphere derived 14C error	Reservoir age offset	Reservoir age offset error
Shallow (1-B-66, 1-B-63)	2686	71	2008	72	678	101
Deep (4-C-5, 4-C-14)	10169	98	8840	108	1329	146

Supp. Table 1. The ages and associated offsets of the ^{210}Pb, ^{137}Cs and ^{14}C dates used for the age model (Fig. 1A). The estimated reservoir ages (C) are used to correct for the ^{14}C ages of the macrophyte macrofossil remains.

Compound class	Compound	Compound class	Compound
Alcohol	1-Dodecanol, 2-hexyl- (C18:0)		1H-Pyrrole-2,5-dione
	Behenic alcohol		Benzyl nitrile
	Ethanol, 2-(octadecyloxy)-		3-Pyridinol, 6-methyl-
Aldehyde	Tetradecanal		Benzenepropanenitrile
Alkane	Heneicosane (C22:0)		Indole
Alkene	6-Tridecene (C13:1)		Diketodipyrrole
	1-Docosene (C22:1)		cis-Cyclo(L-Ala-L-Pro)
Carbohydrate	Furfural		Cyclo(Pro-Gly)
	Furan, 2,3-dihydro-2,5-dimethyl-		Cyclo(Pro-Pro)
	2-Furancarboxaldehyde, 5-methyl-		Alkylamide2
	2-Furancarboxaldehyde, 5-methyl-		Cyclo(Pro-Lys-NH3)
	2-Cyclohexen-1-one, 4-hydroxy-	PAHs	p-Xylene
	4-hydroxy-5,6-dihydro(2H)-pyran-2-one		Ethanone, 2,2-dihydroxy-1-phenyl-
	D-Limonene		1H-Indole, 3-methyl-
	Dianhydrorhamnose		2H-1-Benzopyran-3,4-diol, 2-(3,4dimethoxyphenyl)-3,4-dihydro-6-methyl-, (2α,3α,4α)-
	Benzofuran, 2,3-dihydro-		Butan-2-one, 4-(3-hydroxy-2-methoxyphenyl)-
	3-Acetamidofuran	Phenol	Phenol
	Methyl-α-d-ribofuranoside		p-Cresol
	1,6-Anhydro-β-d-talopyranose		Phenol, 2-methoxy-
	Levoglucosan		Phenol, 3-ethyl-
	Methyl N-acetyl-d-glucosamide		Creosol
Ester	Decanoic acid, decyl ester		Phenol, 4-ethyl-2-methoxy-
	Dodecanoic acid, tetradecyl ester		2-Methoxy-4-vinylphenol
	Decanoic acid, decyl ester		Phenol, 2,6-dimethoxy-
	Dodecanoic acid, tetradecyl ester		Phenol, 2-methoxy-5-(1-propenyl)-, (E)-
	Dodecanoic acid, hexadecyl ester		Phenol, 2-methoxy-4-(1-propenyl)-
	Dodecanoic acid, tetradecyl ester		Phenol, 2,6-dimethoxy-4-(2-propenyl)-
	Tetradecanoic acid, hexadecyl ester		4-((1E)-3-Hydroxy-1-propenyl)-2-methoxyphenol
Fatty Acid	2-Pentenoic acid (C5:1)	Chlorophyll	Prist-1-ene
	n-Hexadecanoic acid (C16:0)	Sterane	Cholesta-3,5-diene
	Octadecanoic acid (C18:0)		Stigmastan-3,5-diene
	2-Heptadecanone (C17:1)	Other	Friedelan-3-one
Hopene	22,29,30 trisnorhop17(21)-ene		γ-Tocopherol
	Urs-20-en-16-one		
Ketone	2-Heptadecanone (C17:1)		
	2-Pentadecanone		
	2-Nonadecanone		
Lignin	Syringaldehyde		
N-compound	1H-Pyrrole, 3-methyl-		
	dl-α-Methylglutamic acid		
	4(3H)-Pyrimidinone, 3-methyl-		

Supp. Table 2. The molecular composition (compound) of the Py-GC/MS compound classes.

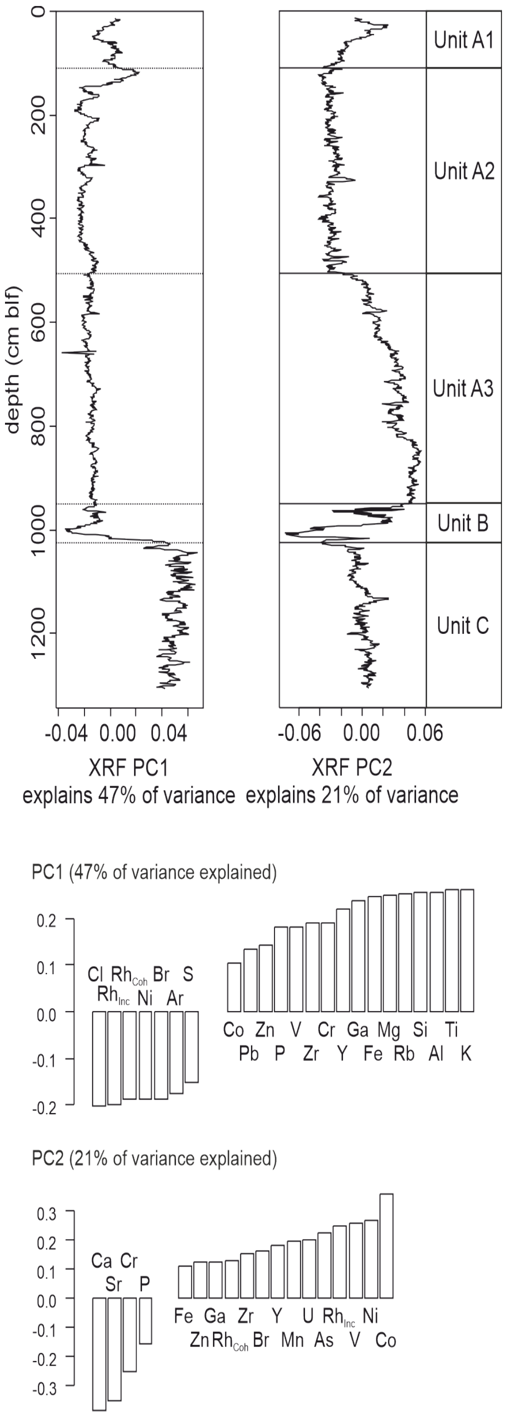

Supp. Fig. 1. Values of PC1 and PC2 with depth, based on a principle component analysis of the standardized fractional abundances of XRF-based elemental composition. The percentage of variance explained is indicated. The lower panels indicate the score of the elements on PC1 and PC2, respectively

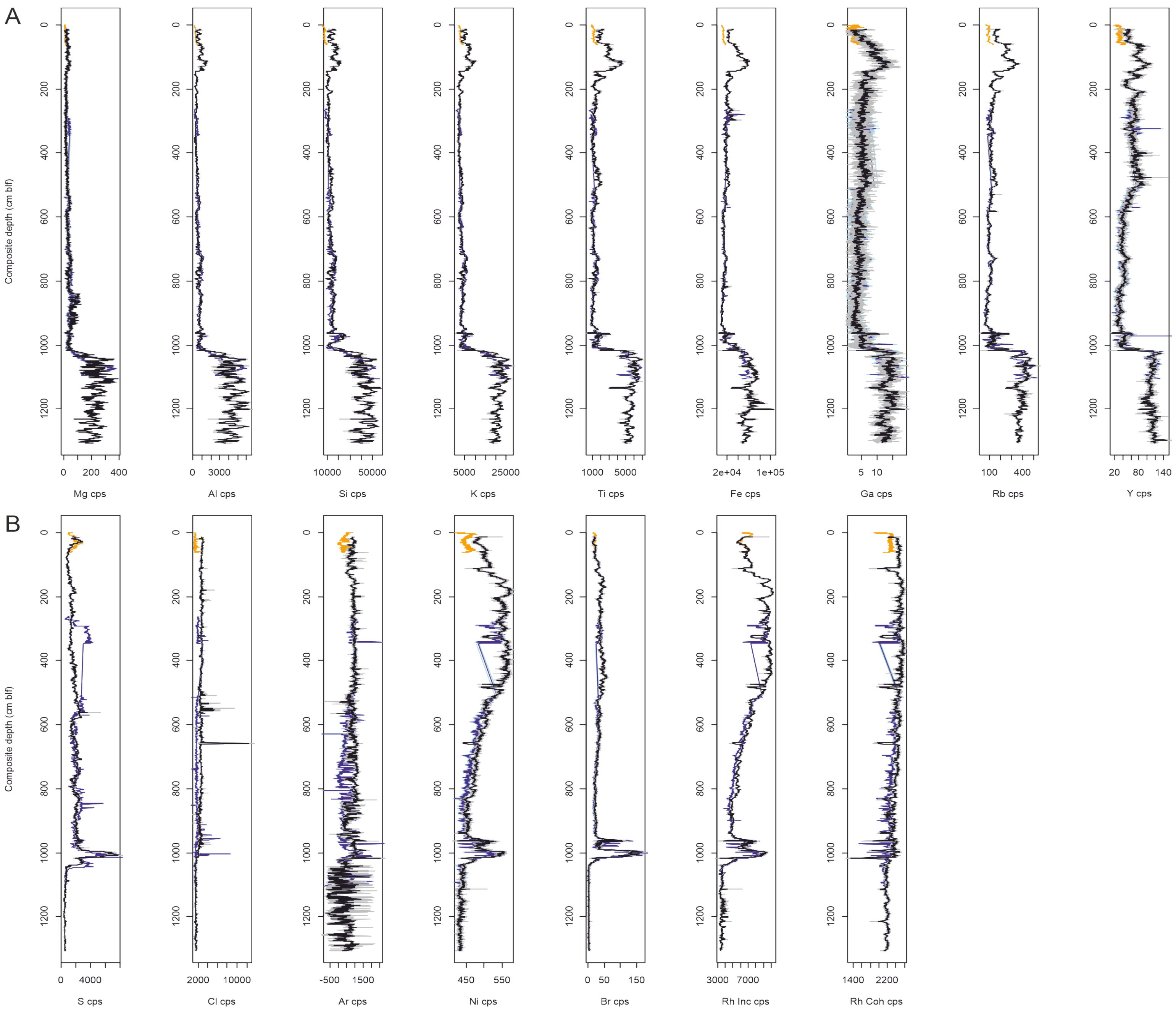
A
B
Composite depth (cm blf)
0
200
400
600
800
1000
1200
Mg cps
0 200 400
Al cps
0 3000
Si cps
10000 50000
K cps
5000 25000
Ti cps
1000 5000
Fe cps
2e+04 1e+05
Ga cps
5 10
Rb cps
100 400
Y cps
20 80 140
S cps
0 4000
Cl cps
2000 10000
Ar cps
-500 1500
Ni cps
450 550
Br cps
0 50 150
Rh Inc cps
3000 7000
Rh Coh cps
1400 2200

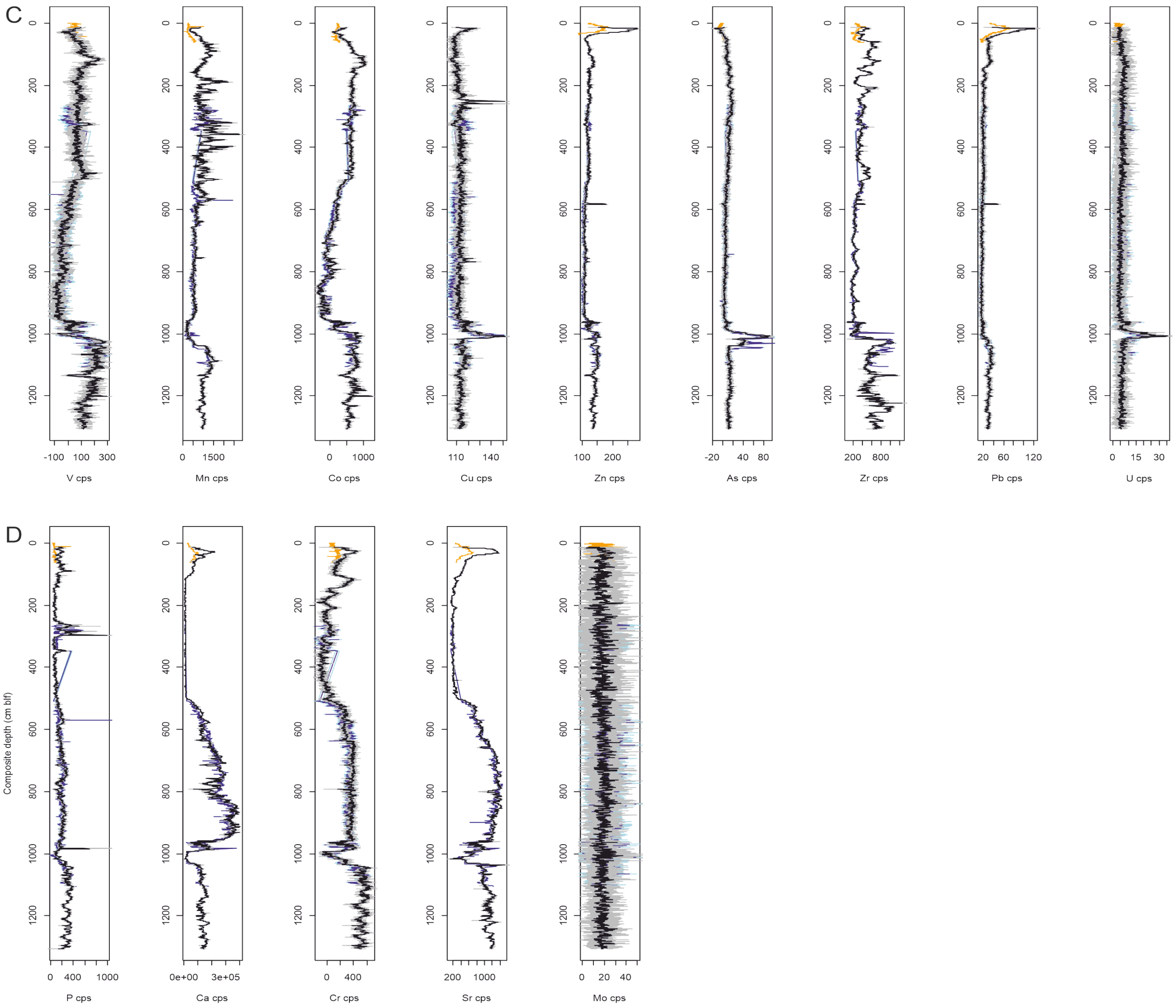

Supp. Fig. 2. The XRF counts of all analysed elements, grouped per score on the first two principle components (Supp. Fig. 1). A: high score on PC1, B: low score on PC1, C: high score on PC2, D: low score on PC2

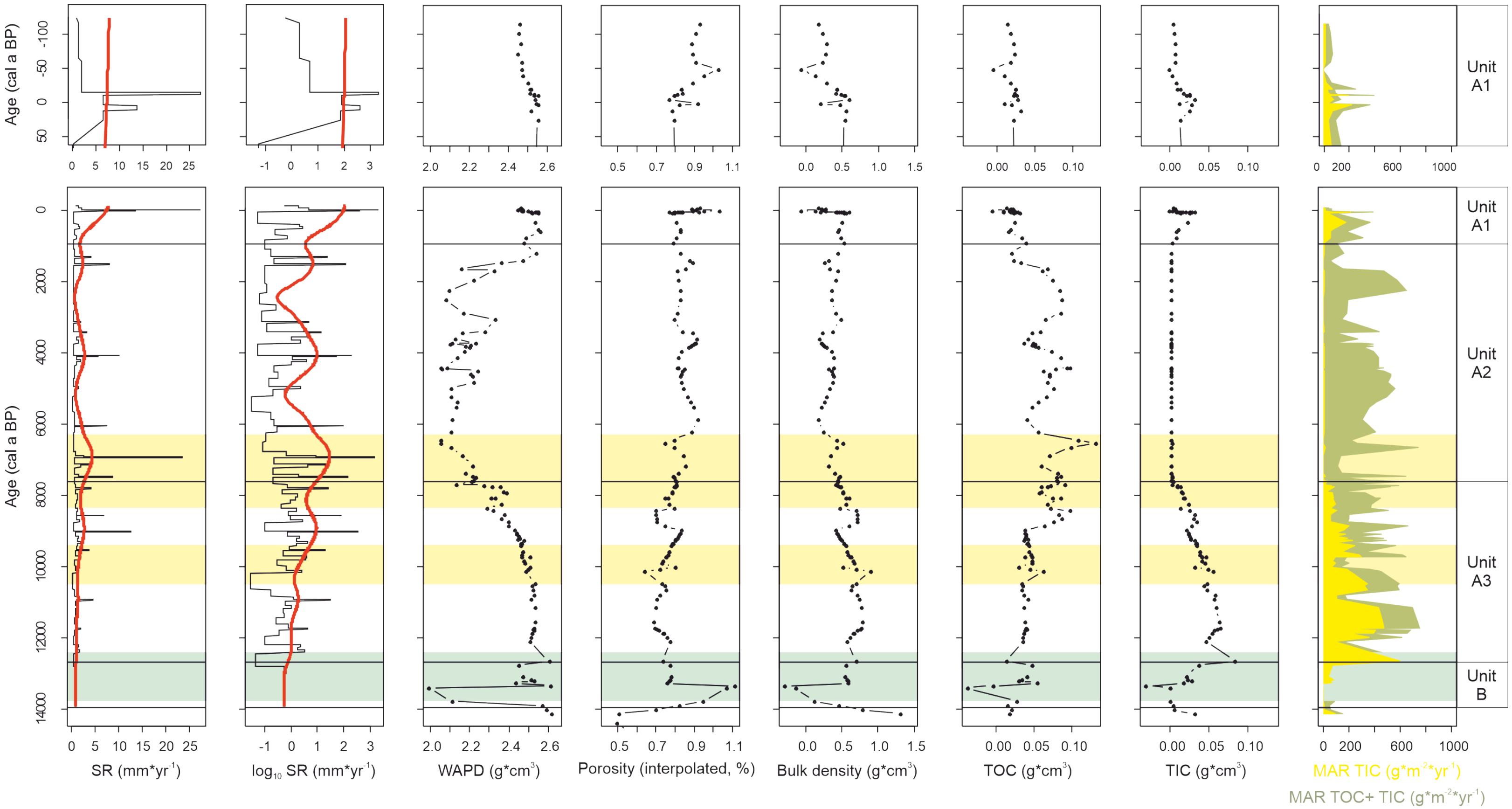

Supp. Fig. 3. The downcore values of the modeled and interpolated parameters, weighted average particle density (WAPD), interpolated porosity, dry bulk density, total organic and total inorganic content of bulk sediment volume, that are at the basis of the calculated MAR rates for total inorganic carbon (TIC) [yellow area] and summed TIC and total organic carbon (TOC) [green area]. The most recent 100 years are replotted on a more detailed scale.

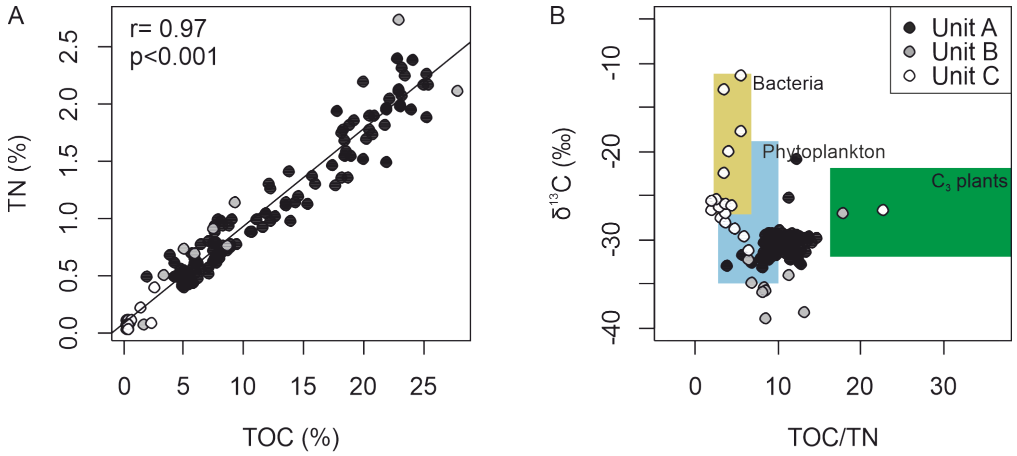

Supp. Fig. 4. Bulk organic matter parameters, A) scatterplot of TOC (%) and TN (%) and B) δ13C-TOC and C/N plot after Meyers et al. (1997). Colored areas indicate organic matter provenance brackets after Lamb et al. (2006).

Meyers PA (1997) Organic geochemical proxies of paleoceanographic, paleolimnologic, and paleoclimatic processes. Organic Geochemistry 27:213–250. https://doi.org/10.1016/S0146-6380(97)00049-1

Lamb AL, Wilson GP, Leng MJ (2006) A review of coastal palaeoclimate and relative sea-level reconstructions using δ^{13}C and C/N ratios in organic material. Earth-Science Reviews 75:29–57. https://doi.org/10.1016/j.earscirev.2005.10.003

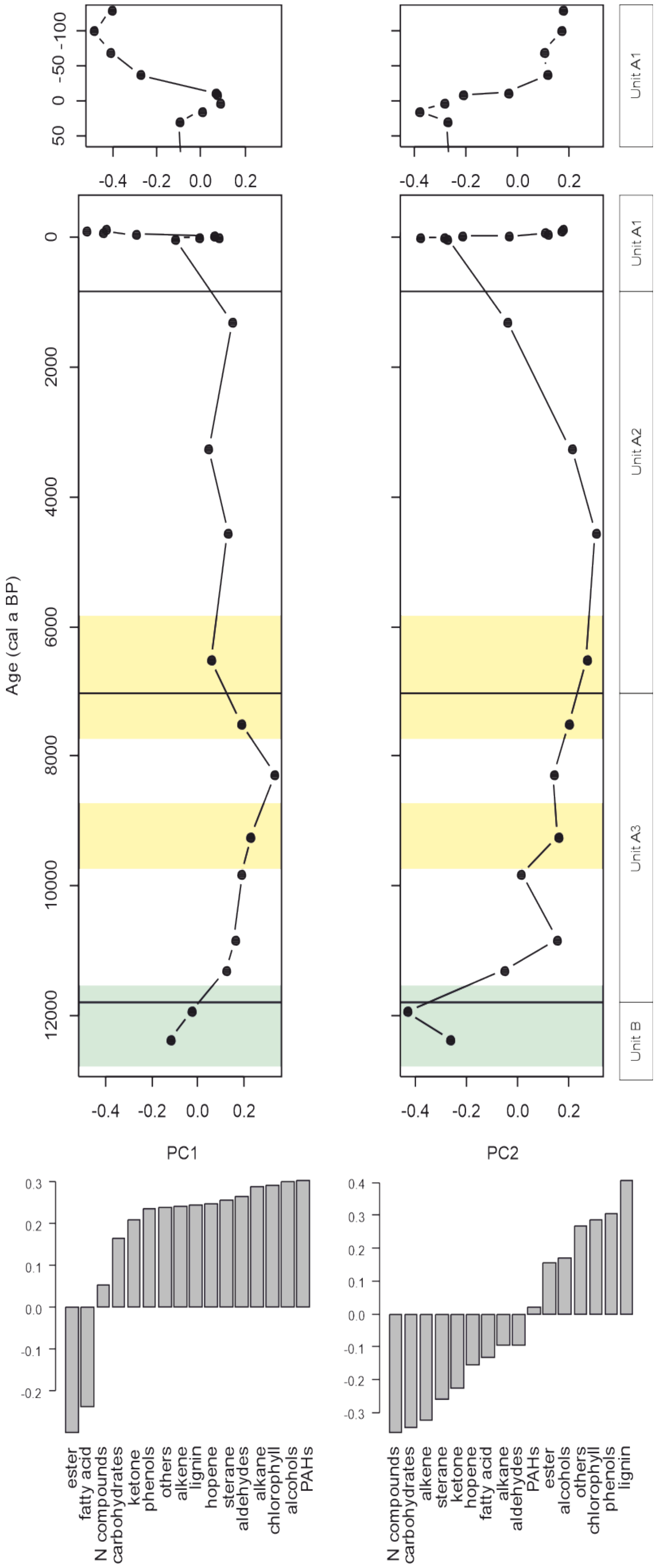

Supp. Fig. 5. The downcore scores of the principal components of variation based on the standardized relative abundances of the compound classes (Fig. 4), with the loading of the individual compound classes on PC1 and PC2 represented by barplots. Background colors indicate climate periods, with Younger Dryas indicated in green and Holocene warm periods indicated in yellow. The most recent 100 years are replotted on a more detailed scale.